

Check for updates





Steel Plates Subjected to Localised Blast Loading: Transient Measurements Using Ultra-High-Speed Camera Technology

R. J. Curry¹ D | G. S. Langdon¹ D | A. Tyas^{1,2}

¹School of Mechanical, Aerospace and Civil Engineering, University of Sheffield, Sheffield, UK | ²Blastech Ltd., Sheffield, UK

Correspondence: R. J. Curry (r.curry@sheffield.ac.uk)

Received: 20 February 2025 | Revised: 9 September 2025 | Accepted: 24 September 2025

Funding: This work is supported by the Engineering and Physical Sciences Research Council (EP/V007637/1).

Keywords: blast | DIC | structural response | ultra-high-speed imaging | uncertainty

ABSTRACT

In this paper, we chart a path to a method that enables us to extract temporal and spatially varying pressure loading effects on the transient response of steel plates under near-field blast loading, employing ultra-high-speed cameras and DIC to measure the transient deformation field. The study addresses the challenges of obtaining full-field, high-fidelity DIC measurements in extreme blast environments by conducting small-scale detonations in close proximity to steel target plates using two ultra-highspeed camera systems. A comprehensive error analysis of these systems is reported and challenges the historic norms of reported accuracy and repeatability in such testing, showing that errors as low as 0.01 mm can be achieved in transient measurements. Pressure measurements obtained via non-contact DIC are compared with data from Hopkinson pressure bar measurements, providing cross-validation of the methods. This research highlights the critical influence of several factors on the reliability of the results, including the chosen camera system, the geometry of the target plate and the errors introduced during DIC processing. The study demonstrates that, with careful attention to experimental design, short exposure times, thorough error evaluation for each camera system and consideration of the structural response, blast test results from DIC can be independent of the camera system used. Furthermore, the study finds that the design of the plate for obtaining accurate impulse distributions is more critical than the inherent camera system uncertainties. Within these limitations, the spatial distribution and temporal development of the impulse loading inferred from the DIC velocity data shows excellent correlation with direct measurements of impulse applied to a nominally rigid target by an identical explosive detonation. This offers a path to a method that could achieve the hitherto impossible task of extracting accurate data on the blast load applied in the extreme nearfield to deforming targets.

1 | Introduction

Digital image correlation (DIC) is a well-established tool that is constantly being improved and adapted to be utilised in different applications. Blast loading from high explosive detonations is a pervasive global threat. Understanding blast loading enables protection systems and urban infrastructure to be safely and sustainably developed and allows policy makers and urban planners to manage the associated risk of harm. The research community has a good understanding of the mechanisms of blast from farfield free-air conventional high explosive detonations. Analytical methods for predicting blast loading on a structure exist, for example [1, 2], and are good for simple target geometries, when the propagating air-shock is dominant, and for hemispherical or spherical charges that are either detonated while on the ground or in free air, respectively [3, 4]. The loading in the far field is idealised as a temporally varying Friedlander shock wave that is spatially uniform across the structure (although corrections for

This is an open access article under the terms of the Creative Commons Attribution License, which permits use, distribution and reproduction in any medium, provided the original work is properly cited.

© 2025 The Author(s). Strain published by John Wiley & Sons Ltd.

1 of 28

clearing are used; see [3, 5]). However, these simplifications seldom apply in real life, as most loading is not ideal: It is spatially non-uniform and temporally varying due to, for example, the use of non-spherical charges [6], the presence of obstacles [7], structural geometry [8] or materials [9]. Transient structural response, complex failure modes and early-time material fractures further compound the difficulties.

Clarke et al. [10–12] employed a two-dimensional array of 17 Hopkinson pressure bars to measure the blast loads arising from the detonation of high explosives in air and those buried at different depths in soil. The system, known as the Characterisation of Blast Loading (CoBL) facility, was found to produce repeatable and accurate pressure measurements at each bar location [10] and could be processed to obtain spatial impulse distribution maps across a near-rigid target plate over a 200 mm diameter [10, 11, 13]. The work by Clarke et al. has previously been shown to be the most accurate way to predict the pressure loading in the near field extreme temperature and pressure environment where conventional instrumentation would be destroyed.

The 10-mm-diameter, 3.25-m-long bars in the CoBL facility are positioned at a centre-to-centre distance of 25 mm, limiting the spatial resolution of the system. To improve the spatial and frequency resolution of the Hopkinson pressure bars' signals and obtain more accurate pressure and impulse distributions for the extreme near fields, Barr et al. [14] reported on the development of the Mechanisms and Characterisation of Explosions (MaCE) facility, with 4 mm diameter maraging steel Hopkinson bars placed at a centre-to-centre distance of 12.5 mm, albeit with the pressure measured over a smaller near-rigid plate area (100 mm diameter). The MaCE system was shown to record higher frequency characteristics of the loading and measure higher magnitude pressures in the central region, important in the extreme near field but less significant at larger stand-off distances.

An earlier work determined an impulse distribution from a velocity field imparted to a deformable plate made from Domex 355MC steel [15] subjected to blast loading [13, 16] using cameras running at a slow speed of 40 kfps allowed for a single data point of plate velocity to be determined. This extended previous work [17] using stereo-imaging systems in combination with a 3D DIC technique to measure transient deformation. However, questions were raised about the temporal resolution as only one data point was available in previous work due to equipment restrictions.

The general use of 3D DIC as a measurement technique is well established across a range of disciplines; see Sutton et al. [18, 19]. In blast applications, Fourney et al. [20] showed that it might be possible to use a 3D DIC system to measure the transient response of test plates under explosion loading. Although velocity and acceleration profiles were recorded, the camera resolution, lighting conditions and depth of field necessary created challenges. Tiwari et al. [21] also used 3D DIC and stereo-imaging to obtain transient out-of-plane deformation and were able to detect a deformation wave moving radially outward from the plate centre although the speed and resolution were still limiting factors.

Aune et al. [22] successfully obtained the transient response of square plates subjected to loads generated by detonating small spheres of C4 explosive at varying stand-off distances. However, there were paint speckle adhesion issues for closer stand-off distances, and limited data was obtained. The frame rate (21 kfps) was able to capture transient features of the response, including plastic waves moving between the plate centre and the boundary. The impulse values used in the paper to describe the deformation of plates were inferred from pressure sensor measurements during a separate set of calibration tests and not from the experimental series or the plate response itself. This approach increased the number of experiments required and could lead to issues for detonation events that result in highly variable loading.

Curry and Langdon [17] used 3D DIC and stereo-imaging cameras filming at 30 kfps to obtain transient deformation across a central strip of a circular steel plate subjected to blast loads. The system was mounted to a blast pendulum, allowing for an estimate of the global impulse (but not its spatial distribution) and the transient response. Follow-up work [23] employing the same experimental arrangement, but this time combined with numerical modelling, examined the influence of charge backing on impulse and transient plate response. The impulse characteristics were inferred from modelling as the lighting available limited the accuracy and resolution of the velocity field measurements.

Improved lighting was used in experiments reported by Rigby et al. [13]. This enabled the use of DIC to obtain impulses from blast tests on deformable steel plates across a central strip; the data was compared to scaled CoBL data (obtained at larger charge masses so it had to be scaled down). Repeatable and consistent results were obtained for the scaled spherical charge detonations, and consistently similar levels of variation were observed in cylindrical charge detonations. The DIC method offered potential advantages over the CoBL system as measurements were not limited to discrete (bar) locations.

As DIC has become prevalent, the importance of a standardised approach to reporting the different test arrangements and processing parameters has become apparent. The International Digital Image Correlation Society (iDICS) was launched to promote and foster best practice and standardisation of DIC for conventional applications. These practices [24] highlight the importance of transparency in reporting measurement error, noise and certainty. However, using DIC in high- and ultra-high-speed imaging for blast applications has unique challenges, especially with respect to lighting and camera selection.

While achieving a completely 'error-free' DIC analysis is impossible, there are ways to reduce errors and increase the reliability of results. The most crucial and controllable aspect is speckle pattern optimisation [25]. This can be achieved through laser engraving

or other automated methods to produce a pattern with even black-to-white coverage, no directionality and speckles sized from 3 to 6 pixels [26]. Selection of subset size is also critical as it dictates the balance between spatial resolution and noise suppression [27, 28]. Users must understand the theoretical basis of speckle evaluation and the limitations of evaluation metrics [26]. Numerical simulations of speckle pattern deformation are recommended for comparing the performance of different preparation methods and identifying optimal parameters if possible [29].

In more recent work, Kaufmann et al. [30, 31] deployed a transient deformation technique using deflectometry on polished steel plates exposed to loading from a gas shock tube and a wave tank. This technique relies on the elastic properties of the plate's deformation to determine very small deflections of the plate. The maximum pressures measured with these techniques using deflectometry are only in the region of 40 kPa in the shock tube experiments and are limited by the elastic limit of the plate when the technique typically ceases to work. The low pressures range makes this technique limiting in near-field blast loading where the pressures and environment are significantly higher and more extreme. Efforts to overcome these limitations by employing thicker plates to limit yield would still result in localised yield of the plates in the areas nearest the blast.

Investigations into plate deformations under shock tube loading have also investigated the fluid structure interaction (FSI) while the plate is being loaded and deforming. This typically results in a small drop in the pressure driving the plate's deformation. Experimental work that uses explosives in near-field blast loading involves the complex loading zone where the shock front has not yet detached from the fireball described by Tyas et al. [32]. No literature has yet been able to illustrate FSI effects, like those illustrated in better characterised work on air- or water-loaded plates, to any reduction in loading of plates loaded by explosives in the nearfield where the fireball interacts with the plate.

Spherical and cylindrical charges are two common configurations used to load deformable structures [4, 13, 33–36]. The clear distance between the charge face and the deformable structure is typically specified. When differences were observed between the deformed structures, they are often attributed to loading that has been numerically predicted (e.g., [37]). Direct measurements of the pressure loading are challenging in the extreme near field, and the final deformed shape has often been a common way to distinguish or infer features of this loading.

In this paper, results from blast tests on steel plates with transient data obtained from improved stereo-imaging systems are reported. The data was processed using DIC to obtain transient velocity fields and deformation profiles across nearly the entire surface of a blast-loaded steel plate (as opposed to just a central strip of [17]). The possible sources of error in the transient measurements are evaluated by comparing the responses obtained using two different camera systems capable of ultra-high speeds with results from identical (i.e., not scaled) tests performed using CoBL. The near-field nature of the blast event generated a spatially non-uniform pressure load across the plates. The implications of this for the velocity field and plate response are discussed, showing the need for careful consideration of the structural response characteristics of the plates chosen for this type of testing when the goal is to obtain an impulse distribution arising from the loading separate from the plate behaviour. This method provides a way for blast engineers to validate the spatio-temporal specific impulse causing the deformation of near-field blast-loaded plates.

2 | Experimental Approach

To improve rigour, two different measurement techniques were used to allow for cross validation of the measured impulses. The first approach employed the CoBL apparatus to determine the pressure loading (using an array of Hopkinson pressure bars to measure the pressure at discrete points). The second platform used stereo high/ultra-high-speed cameras and DIC to obtain the transient behaviour of blast-loaded clamped steel plates to infer a specific impulse across the rear plate surface.

2.1 | Blast Loading

For both experimental platforms, near-field air-blast loading was generated by detonating PE10 plastic explosive charges using Euronel 2 non-electrical detonators. The charges were positioned and supported using polystyrene bridges, such that the centre of the charge was aligned with the plate centre as shown in Figure 1a. The length of the bridge legs was adjusted to create the desired stand-off distance, defined as the clear distance between the charge and the plate surface. The bridges were attached to the plate on the clamp boundary with a small piece of double-sided tape, meaning they were blown off during the detonation, which minimised their effect on the central loading from the area of interest.

For the majority of tests, the charges comprised 38-mm-diameter cylinders (as seen in Figure 1b). The height of the cylindrical charges was varied with explosive charge mass, whereas the charge diameter was kept constant, following previous work [16, 17, 23, 38]. The very fast high-pressure expansion of the detonation products (in the order of ~4500 m/s) generates a shock wave that expands outward from the rear [32]. A small number of DIC experiments used spherical charges to compare the results with a less centrally concentrated loading pattern.

Strain, 2025 3 of 28

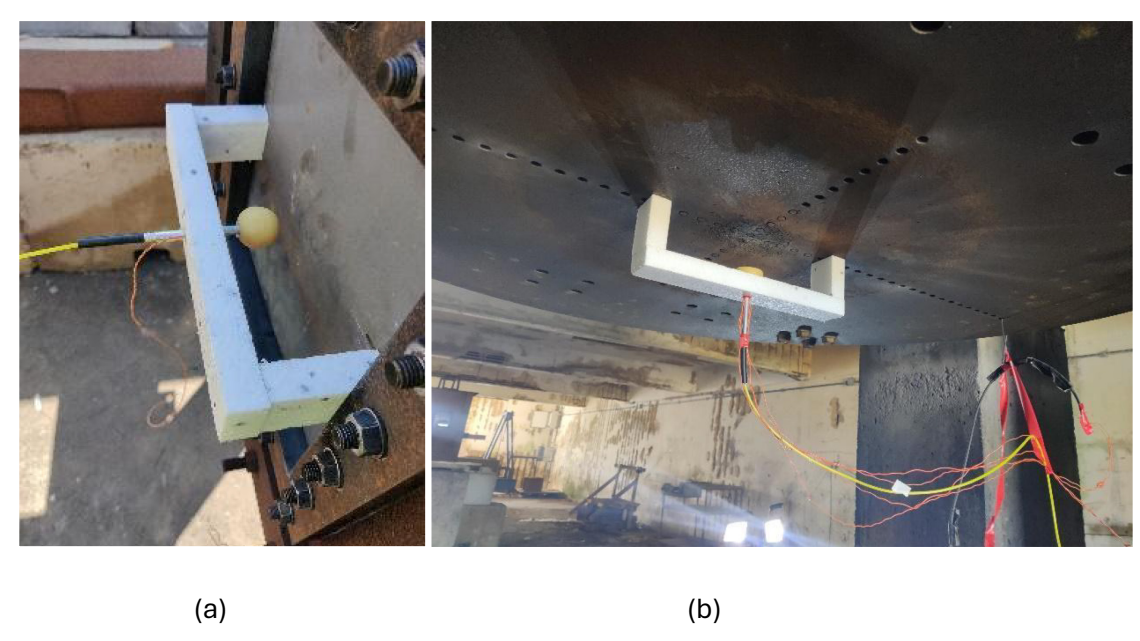


FIGURE 1 | Photographs showing charge positioning, detonator location and polystyrene bridge supports. (a) DIC test, spherical charge. (b) CoBL test, cylindrical charge (length of polystyrene bridge in both images is 300 mm long for scale).

2.2 | CoBL Pressure Measurements

Three experiments were performed using the CoBL test platform, with the charge positioned such that it was centrally located at a stand-off distance of 50 mm (see Figure 1b). Seventeen Hopkinson bars were mounted in an array at radial distances of 25, 50, 75 and 100 mm in a cross formation with one central bar (radial ordinate of 0 mm). This resulted in 17 discrete pressure measurement positions to characterise the spatial and temporal pressure loading imparted to the near rigid plate in the CoBL frame during each charge detonation. A schematic of the CoBL test platform is shown in Figure 2.

Charge masses were limited to 20 and 30 g to ensure the pressures produced in the centre of the array would be below the yield stress of the measurement bar material (650 MPa), given the close proximity of the charge to the bars. Data for individual bars was processed to determine the temporal pressure loading, and the full spatial loading map from each test was obtained by combining the results from each bar location. The spatial maximum specific impulse results are used as baseline data for comparison with the DIC results. The results are summarised in Table 1. The repeated 20 g detonations show remarkably good consistency in terms of pressure pulse shapes and the magnitudes of maximum specific impulse and peak pressure.

Figure 3 shows graphs of pressure versus time and cumulative specific impulse with time, for each radial ordinate (compared to the central bar output). The maximum specific impulse values versus radial plate ordinate were plotted on a single axis to produce a combined map of impulsive loading imparted on the rigid plate in the CoBL rig, as seen in Figure 3e. As expected, the central bar (directly above the charge centre) recorded the highest pressures, with magnitudes of approximately 500 and 520 MPa for the 20 and 30 g detonations, respectively. The peak pressures decayed rapidly as radial ordinate increased, moving radially outwards from the charge location. The shape and magnitudes of the specific impulses generated (Figure 3a–d) were similar in form to those obtained in previous work [13].

The CoBL platform is a reliable measurement system for recording reflected pressures using an array of Hopkinson bars, but some comments on its limitations are in order. The resolution of the measurements was limited by two factors, namely, (1) the 10 mm bar diameter, which leads to a tendency (through Pochhammer–Chree dispersion mechanisms) to lose the sharpness of the actual load-time signal, and (2) the discrete number of data points and their positions, which are limited by the number of bars and their fixed locations. The former limits the fidelity of fine detail in the pressure–time signal that can be captured although broadly the temporal development of cumulative specific impulse is well characterised (see [14]). Generally, for the scenarios covered in this study, it would be assumed that the target response is dominated by the impulse imparted. This will be investigated in Section 3.5. The latter limitation was partially overcome by interpolating the loading between radial positions.

Additionally, it is well established that as the detonation fireball expands violently, turbulent structures can form which can cause large spatially localised variations in loading, although the total impulse applied over a large area is relatively consistent in nominally identical tests [39]. These variations are randomly distributed and inherently unpredictable. Although the four records at each of 25, 50, 75 and 100 mm radial offsets can be averaged to partially address this issue, the existence of only one central bar means that the record is not necessarily representative of the load expected in repeat tests. This is reflected in the data presented in the first two rows of Table 1.

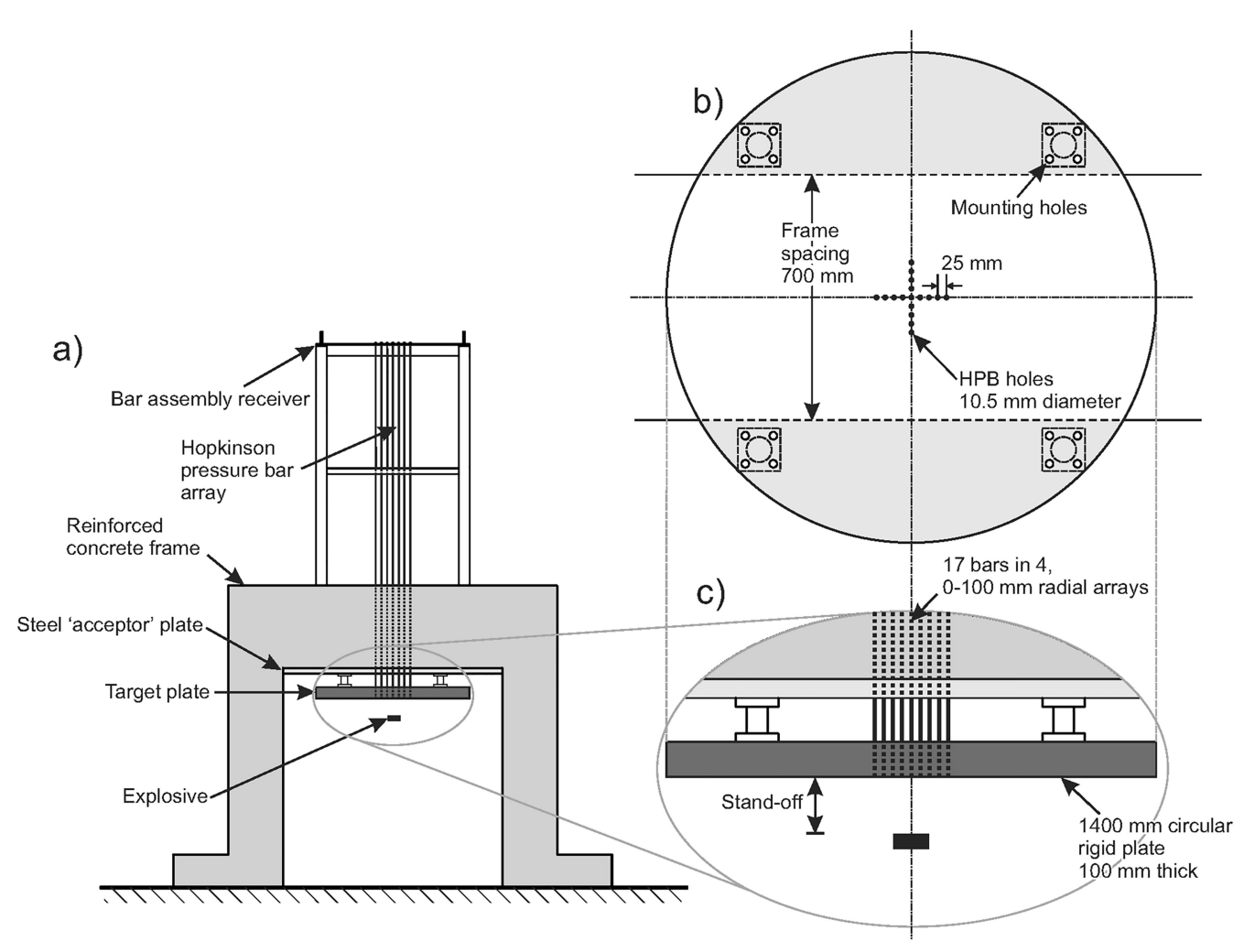


FIGURE 2 | Schematic of CoBL platform, showing (a) plan view, (b) top view of near-rigid face plate showing bar array and (c) zoomed side view showing flush-aligned bars with the face plate.

TABLE 1 | Summary of CoBL test results of 38 mm cylindrical charges at 50 mm SOD.

		Average specific impulse at radial ordinates (MPa.ms)					
Test designation	Mass of PE10 (g)	0mm	25 mm	50 mm	75 mm	100 mm	Total impulse (Ns)
22042022-1	20	7.99	2.42	0.56	0.13	0.09	20.8
22042022-2	20	7.21	2.70	0.58	0.13	0.09	21.0
22042022-3	30	8.47	3.20	0.78	0.21	0.13	27.3

2.3 | DIC Plate Test Measurements

2.3.1 | Specimens

The DIC plate approach used a 3-mm-thick Strenx 700 steel plate, fully clamped into a rigid frame, as shown in Figures 1a and 4. The plates were square with a side length of 400 mm and an exposed side length of 300 mm. Twenty 15-mm-diameter equi-spaced bolt holes were laser-cut into the periphery of the plate, with a tolerance of 0.2 mm, to facilitate mounting in the clamp frame. Strenx 700 is a high-strength structural steel with a minimum yield strength of 700 MPa and a maximum carbon composition of 0.12% (SSAB sheet 2022). It was selected due to the high tolerance on its chemical composition (with small quantities of alloying elements, inter alia, of manganese, silicon and phosphorus) ensuring a repeatable material response.

Strain, 2025 5 of 28

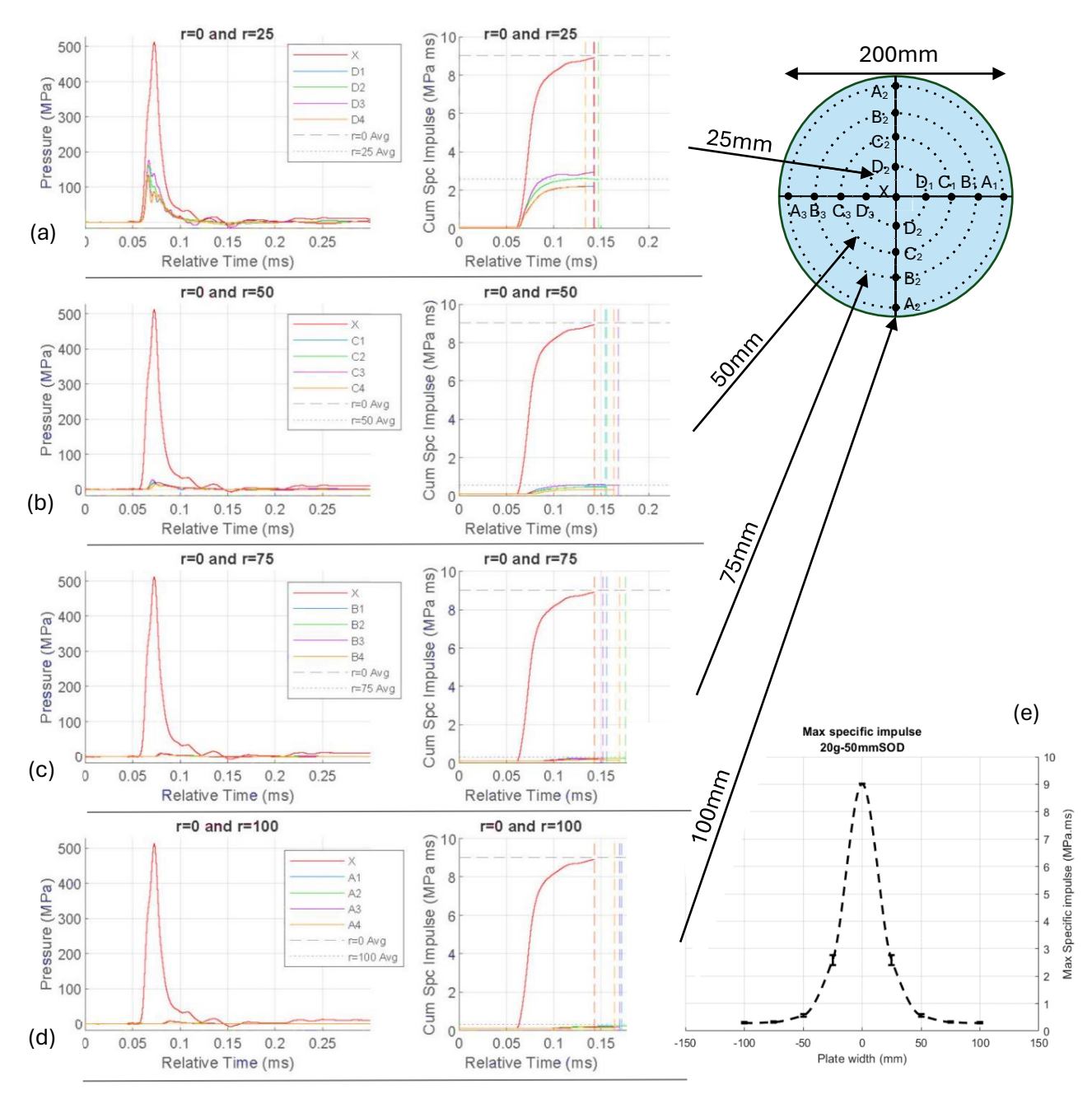


FIGURE 3 | The specific impulses and pressure–time histories obtained from the CoBL bar data (compared to the central bar 'X') at radial distances of (a) 25 mm, (b) 50 mm, (c) 75 mm and (d) 100 mm and the (e) spatial representation of maximum specific impulse at radial ordinate values.

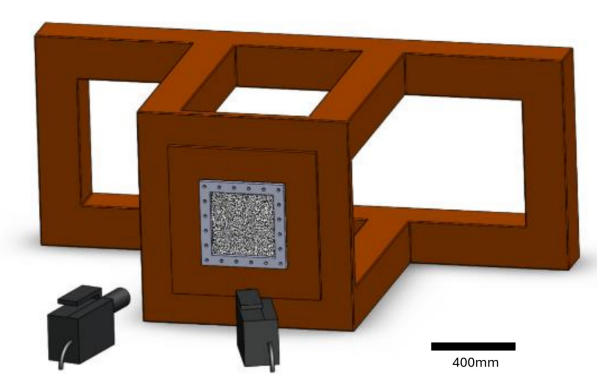


FIGURE 4 | Scaled schematic showing steel test plate clamped in rigid clamping frame, with cameras mounted to film the response of the rear (non-loaded) speckled surface of the test plate. Plate edge length of 400 mm.

2.3.2 | Blast Loading Arrangement

A total of 22 tests were performed. Six used spherical charges (#16–21) varying between 30 g and 60 g of PE10 and stand-off distances in the range of 20–50 mm (see Table 2). Sixteen cylindrical charge detonations (#1–15 and #22) were performed for stand-off distances ranging from 0 to 50 mm and charge masses between 10 and 40 g.

The rear surface of each test plate was sand-blasted to roughen the surface and remove contaminants. The cleaned plates were painted with a thin layer of white paint, and a random speckle pattern was applied using an ink roller. The speckle pattern size was selected to match the camera resolution and area of interest with between 6 and 9 pixels per speckle according to the iDIC best practice guide [24]. The tests were filmed using two high-speed cameras positioned approximately 2 m from the test plate with an included angle of 35°.

2.3.3 | Camera Systems

Two different camera systems both using Samyang 135-mm fixed focal lenses were used to capture the deformation and response of the plates. Lens distortion was accounted for in the bundle adjustment as part of the calibration process. This enabled a comparison between two stereo-camera systems to evaluate the influence of the camera type on the obtained measurements. The first system was a pair of Shimadzu HPV-X2 cameras (10 bit, $32\,\mu m$ pixel size, $400\times250\,px$ sensor with $100\,k$ pixels in total). Its main advantage was its high frame rate, capable of up to $5\,Mfps$ at $400\times250\,px$. The resolution was fixed as the frame rate varied, but it was only able to record 128 frames in each recording.

The second system was a pair of 12 bit, $20\,\mu m$ pixel size Photron SA-Z 2100k cameras. These had a much greater maximum resolution, $1024\times1024\,px$ at 1078 fps, but this resolution reduced with increasing frame rate, for example, to $640\times280\,px$ for a frame rate

TABLE 2 | Experimental test matrix.

Test #	Mass of PE10 (g)	SOD (mm)	Charge shape
1	30	50	Cylindrical, Ø38mm
2	30	50	Cylindrical, Ø 38 mm
3	30	50	Cylindrical, Ø 38 mm
1	40	50	Cylindrical, Ø 38 mm
5	20	50	Cylindrical, Ø 38 mm
5	20	30	Cylindrical, Ø 38 mm
7	10	30	Cylindrical, Ø 38 mm
8	25	30	Cylindrical, Ø 38 mm
9	30	30	Cylindrical, Ø 38 mm
10	30	30	Cylindrical, Ø 38 mm
11	30	30	Cylindrical, Ø 38 mm
12	10	15	Cylindrical, Ø 38 mm
13	15	15	Cylindrical, Ø 38 mm
14	20	15	Cylindrical, Ø 38 mm
15	25	15	Cylindrical, Ø 38 mm
22	10	0	Cylindrical, Ø 38 mm
16	30	50	Spherical
17	30	50	Spherical
18	40	50	Spherical
19	60	50	Spherical
20	30	30	Spherical
21	30	20	Spherical

Strain, 2025 7 of 28

of $100\,\mathrm{kfps}$ and a maximum potential frame rate of $2.1\,\mathrm{Mfps}$ at $128\times8\,\mathrm{px}$. For these tests, a frame rate of $100\,\mathrm{kfps}$ was used, giving 179,200 pixels which represents a 79% increase in pixels when compared to the Shimadzu system (when both operating at the same frame rate).

2.3.4 | Lighting

The available lighting limited the exposure time that was used with each camera system. Poorly arranged lighting can create uneven illumination of a speckled surface that will generate errors in image post-processing (and possibly lead to decorrelation due to large uncertainties). For both arrangements, the lights were carefully arranged to evenly illuminate the test plate. By minimising uneven lighting and hotspots, interference with subsequent image processing was drastically reduced. The Shimadzu camera tests used an arc flash bulb, $30\,k$ Luminys light to illuminate the rear surface from a distance of approximately $2.0\,m$. This enabled the Shimadzu system to use a reduced exposure time of $20\,\mu$ sec. The Photron camera tests used GsVitec LED lights positioned approximately $1.0\,m$ from the test plate, out of line with the Photron cameras, enabling an improved minimum exposure time of $8\,\mu$ s. Lower exposure times reduced the potential for motion blur during deformation of the plates.

2.3.5 | Calibration and Noise Characterisation for DIC Plate Tests

A summary of the 3D DIC settings and performance variables employed during the blast tests is shown in Table 3. Although some aspects were the same for both systems, there were differences in the sensor details, field of view (FOV) size and exposure times that resulted in performance differences. For the purposes of this study, the correlation was undertaken in Correlated Solutions VIC-3D 9, and acquisition was undertaken in VIC Snap.

The FOV could not be kept exactly the same for the two camera systems because the number of pixels across the central width varied with camera type (Table 3). The frame rate was kept constant at 100 kfps and was chosen because this gave an ROI of 410 px for the variable Photron system, which was as similar as possible to the fixed value of 316 px for the Shimadzu cameras. This difference was entirely driven by the experimental requirements of calibrating the systems with the physical size of the special low-resolution targets needing to fit around the immovable clamp frame for holding the specimens. Calibrations were conducted immediately prior to each blast experiment. The slight differences in resolution and ROI, due to camera sensor size, meant that a specific calibration target was used for each camera system. For the Photron cameras, calibrations were conducted at full resolution before being operated at a reduced resolution at higher frame rates in the blast tests. These actions minimised distortion correction, cropping, lensing and out-of-plane errors [24].

Combining the above differences between the two camera systems meant that they operate at different magnifications, with the Shimadzu average resolution magnification being $1.18 \, \text{px/mm}$ and the Photron system having a resolution magnification of $1.72 \, \text{px/mm}$

TABLE 3 | Experimental DIC settings and performances.

Technique used	3D stereo image correlation					
Camera type	Shimadzu HPV-X2	Photron SAZ				
Frame rate	100 k	100 k				
Exposure time	20 μs	8 µs				
Subset size	17	29				
Shift	40%	30%				
Subset weights	Gaussian	Gaussian				
Interpolation function	Optimised 8-tap	Optimised 8-tap				
Correlation criterion	Normalised squared difference	Normalised squared difference				
Smoothing applied to images	None	None				
Sensor details	10 bit, 32 μ m pixel size, 400 \times 250 px sensor	12 bit, 20 μ m pixel size, 1024 \times 1024 px sensor				
Field of view	355×220 mm	412×180 mm				
Resolution magnification	1.18 px/mm	1.72 px/mm				
Smoothing method	Centre weighted	Centre weighted				

TABLE 4 | Noise floor characterisation for the two camera systems.

		Singl	e image		20 images				
Camera	Max SigmaZ (mm)	Std dev SigmaZ (mm)	Max strain	Std dev strain	Max SigmaZ (mm)	Std dev SigmaZ (mm)	Max strain	Std dev strain	
Shimadzu HPV-X2	84.7 e-3	139 e-4	974 e-6	212 e-6	0.0847	101 e-4	1.90 e-3	196 e-6	
Photron SAZ	9.02 e-3	8.99 e-4	348 e-6	814 e-6	0.0081	6.17 e-4	0.648 e-3	88.8 e-6	

mm. Given the differences in spatial resolution at 100 kfps, a 2.5-mm speckle pattern was used for the plates filmed using the Photron cameras, whereas a 5-mm speckle pattern was used for tests employing the Shimadzu cameras.

There are two main sources of error introduced to DIC measurement, namely, image noise and measurement bias. Image noise is typically a result of the inherent variations in the images captured as a result of the experimental setup with aspects like sensor noise, lensing, stereo angle and speckle pattern being the main contributing factors [24, 28]. Bias is the systematic error in the system, typically a result of either poor calibration or possible camera movement during testing (causing a global offset or shift to the data). In this work, both sources of potential error are considered and minimised.

Specimen correlation is achieved by assigning subsets throughout the area of interest that contain unique speckle information. The DIC algorithm tracks where these subsets move by checking for possible matches at several locations and using a similarity score (correlation function) to grade them. The position where the subset has moved to is where the error function would be minimised, allowing for some deviation from the actual position of a specific subset that can be identified and interpreted as noise. Image noise was characterised by analysing the standard deviation of displacement data captured by the camera systems prior to detonation, when there was no movement of the test plate. The noise present in the data was evaluated based on the variation of out-of-plane 'W' displacements between images, these were labelled as 'Sigma_Z' in the analysis and were calculated according to the correlation function shown in Equation (1). From this, the pixel coordinates (x,y) are used together with the displacement disparity (u,v). This considers the image before motion I and finds the difference with the image after motion I* looking for the least squares difference to optimise the position.

$$C(x,y,u,v) = \sum_{i,j=-n/2}^{n/2} (I(x+i,y+j) - I^*(x+u+i,y+v+j))^2$$
(1)

Two different assessments of error were reported this way. The first error assessment is the maximum or minimum variation of a particular quantity of interest (QOI) seen in the stationary plate. This allowed an estimate of the worst possible error bounds that were achievable and were specific to a test, as these included the influence of external factors (such as ambient lighting as well as unique variations in the speckle pattern) that may cause measurement fluctuations.

The second assessment of error was the standard deviation in the displacement measurement of a stationary plate. This was more statistically relevant, reporting the inherent fluctuations observed across the whole plate. When averaged over 20 images, this gave a better way to report the certainty of the measurement systems. These errors are small (see Table 4) but illustrated that the higher resolution Photron SAZ system produced a slightly better error performance.

Figure 5 shows typical maps of noise in the variation of displacement for the two camera systems. The static errors shown in Figure 5 include any local variations that may have occurred when the plate deformed during the experiment (e.g., any changes in lighting or local degradation of the speckle pattern that potentially increase local errors) as these were reported separately in the DIC software as the certainty of each individual facet. These 'Sigma Z' values were used to report the error bounds on individual local measurement points such as mid-point displacement as a confidence interval. As the speckle pattern size is already optimised between the two different camera systems (according to the best practice guide [24]), then the differences in error for the two systems can be attributed to sensor noise, lighting differences and inherent length scale differences of the two systems. Therefore, higher resolution systems have a lower error noise floor for the same area of interest. No additional smoothing or filtering of displacement data was undertaken in this work, and the uncertainty bans were found to be small in comparison to the inter-frame movement during the initial deformation of the plates.

As the uncertainty in the position of any one facet in the analysis varied both spatially and temporally after detonation, five time increments $30\,\mu s$ apart (30, 60, 120, 150 and $180\,\mu s$) were selected, and the reported out-of-plane 'Sigma Z' displacement is shown in Table 5 and graphically in Figure 6 for each one. The uncertainty was small in comparison to the displacement of the plate for each

Strain, 2025 9 of 28

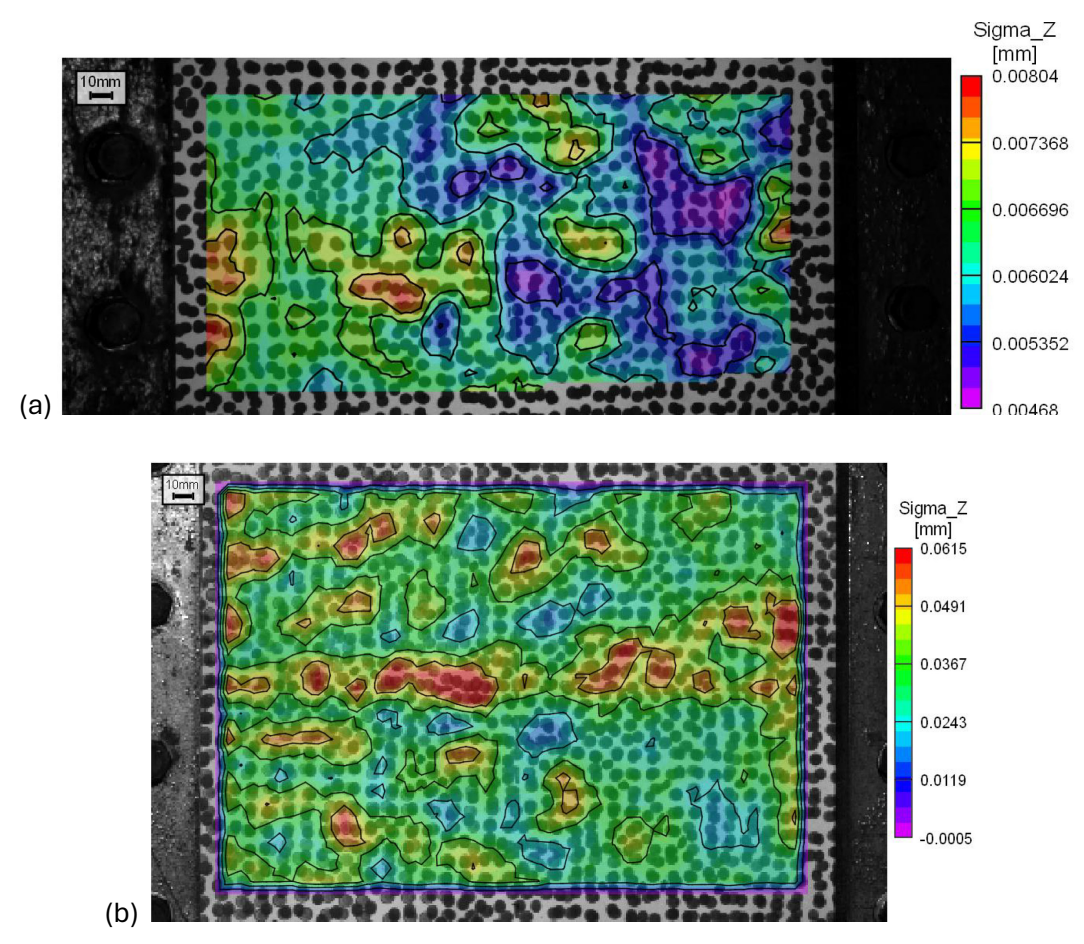


FIGURE 5 | Typical maps of displacement variation noise in each subset measurement across a plate (prior to testing) in the out-of-plane 'SigmaZ' displacement for the (a) Photron SAZ and (b) Shimadzu HPV-X2 cameras.

TABLE 5 | The maximum and first standard deviation Sigma Z uncertainty (measured in mm) for each transient time plotted in Figure 6.

	30 µs		60 µs		120 μs		150 µs		180μs	
Camera	Max	Std dev								
Shimadzu HPV-X2	0.105	0.0155	0.138	0.0178	0.128	0.0187	0.127	0.0192	0.127	0.0196
Photron SAZ	0.0154	0.0015	0.0415	0.0038	0.0496	0.0047	0.0504	0.0054	0.0497	0.0055

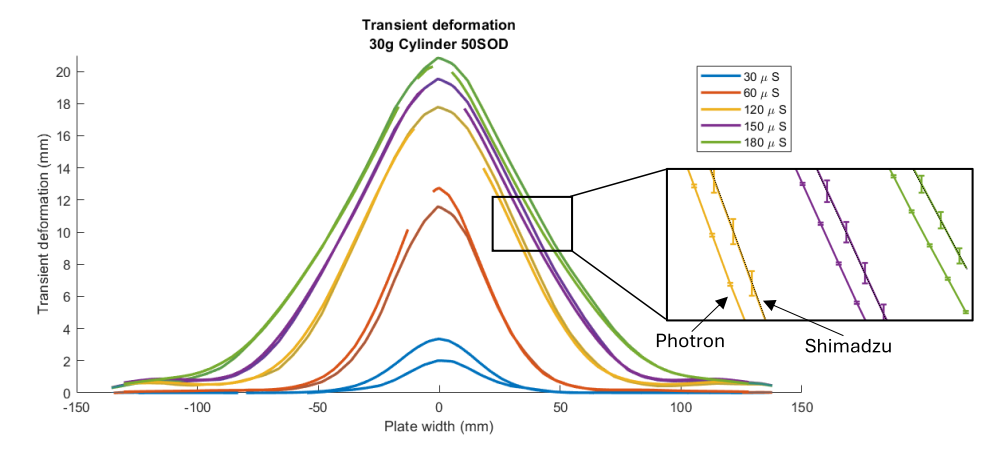


FIGURE 6 | Transient midline displacement plots of the plate and a zoomed-in region of interest showing the uncertainty measure error bars for the two camera systems (inset: Photron system: left, Shimadzu system: right, showing slightly large error bar).

chosen increment. The virtually overlapping profiles for the two camera systems seen in Figure 6 suggest excellent repeatability, and the small error bars indicated the high certainty in the measurements for both camera systems.

In the presented work, the noise was random and of very small magnitude, below 0.14 mm in all cases and as low as 0.01 mm in most tests (Table 5). The worst-case influence of heat haze from the lights was evaluated by positioning the lights directly in front of a speckled test plate and allowing the heat to rise in front of the region of interest. The heat haze rising caused small distortions in the air between the cameras and the test plate, leading to slightly larger variations in displacement across the plates. These were up to approximately 0.3 mm in magnitude but were minimised during blast testing by repositioning the lighting systems away from the optical path of the images, and the resulting tests were then conducted.

3 | Results and Discussion

3.1 | Blast Test Results

Twenty-two blast tests were performed using the DIC plate test approach. Six of the experiments used spherical charges and fifteen used 30-mm-diameter cylinders. The results summary is shown in Table 6. Some of the tests were repeats of each other (namely, 30g tests at 50 mm SOD for both cylindrical and spherical charge detonations and 30g tests at 30 mm for the cylindrical charges). The maximum permanent and peak displacements obtained from these tests under the same conditions exhibited variations of less than half a plate thickness, indicating good repeatability of the loading and response. Two tests resulted in fracture and capping failure in the test plates, rendering peak and permanent displacement values not applicable. In those tests, cap velocity was estimated using DIC.

3.1.1 | Spherical Charge Detonations

The transient out-of-plane displacement contour map of the plate rear surface during the first millisecond of response is shown in Figure 7 for a representative 30 g spherical charge detonation test. The transient mid-line displacement profile of the same plate shown in Figure 8 is effectively a slice through the surface shown in Figure 7 at different time intervals. For the first $150\,\mu s$, Figure 8 indicates that the deformation was nipple shaped (i.e., a localised peak atop a small magnitude global dome shape), initially localised in the centre with an inflexion point, indicating some localisation of the initial blast loading due to the close stand-off distance. The displacement spread out radially towards the boundaries as time proceeded, and the inflexion radial ordinate moved towards the boundary.

Between 150 and $180\,\mu s$, the profile shape changed to a more conical form along the whole plate width, as the inflexion point became less pronounced as it moved radially towards the clamp boundary. Figure 7 shows very little change in mode shape after this, only variation in displacement magnitude. The plates subjected to blast loading from spherical charge detonations all exhibited similar behaviour to that shown in Figure 7. The variations in displacement magnitude and degree of localisation were attributed to different combinations of charge mass and SOD. As expected, more localised response was observed in closer SOD tests, and larger peak displacements were observed for larger charge mass detonations.

The variation in mid-point displacement-time histories for the range of charge mass and SOD combinations is illustrated in Figure 9. The qualitative behaviour of the plates was similar to that observed by Curry and Langdon [17] for blast-loaded fully clamped steel plates, with a large initial rise in displacement due to the impulsive loading followed by a peak displacement after approximately 0.5 ms, with post-peak elastic vibrations about a permanent displacement dominating the response thereafter.

A typical contour plot visualising the transient evolution of the out-of-plane velocity across the plate width is shown in Figure 10. The velocities were relatively low, less than 100 m/s, even in the early phases of the impulse transfer from the blast loading. The velocity was localised in the central region, as expected, due to the close SOD. As time progressed, the velocity map revealed a dominant plastic shear wave travelling out towards the boundary. Two waves are evident: (i) an elastic one that started at the plate centre and propagated radially outwards (towards the clamp boundary) from the point of the initial disturbance and (ii) a plastic wave that followed the elastic one at a slower wave velocity, where following plate theory [40], once the plate deformation exceeded one plate thickness there will be some element of plasticity. The central plate velocity reduced, whereas the location of the peak moved radially outwards until the shear wave reflected from the clamped edge (in the case of the test shown in Figure 10, the wave appears to reflect off the boundary 0.07 and 0.08 ms as seen by the light blue velocity field). Although the clamp frame was not speckled in this study, no detectable frame movement was observed in the test images, and ridged body motions were removed from the DIC data as a precaution.

Strain, 2025 11 of 28

TABLE 6 | Summary of DIC plate test results (HPV-X2: Shimadzu, SAZ: Photron).

Test #	Mass of PE10 (g)	SOD (mm)	Charge shape	Camera type	Max. permanent displacement (mm)	Max. peak displacement (mm)
1	30	50	Cylindrical, Ø38mm	HPV-X2	18.2	26.2
2	30	50	Cylindrical, Ø 38 mm	HPV-X2	18.8	27.7
3	30	50	Cylindrical, Ø 38 mm	SAZ	18.4	27.3
4	40	50	Cylindrical, Ø 38 mm	SAZ	27.6	34.3
5	20	50	Cylindrical, Ø 38 mm	SAZ	15.1	22.9
6	20	30	Cylindrical, Ø 38 mm	SAZ	22.9	30.0
7	10	30	Cylindrical, Ø 38 mm	SAZ	11.5	18.1
8	25	30	Cylindrical, Ø 38 mm	SAZ	27.7	34.7
9	30	30	Cylindrical, Ø 38 mm	SAZ	29.0	36.0
10	30	30	Cylindrical, Ø 38 mm	SAZ	28.8	36.2
11	30	30	Cylindrical, Ø 38 mm	SAZ	28.3	36.2
12	10	15	Cylindrical, Ø 38 mm	SAZ	17.8	23.5
13	15	15	Cylindrical, Ø 38 mm	SAZ	24.1	30.4
14	20	15	Cylindrical, Ø 38 mm	SAZ	28.5	35.8
15	25	15	Cylindrical, Ø 38 mm	SAZ	Fractured	Fractured
22	10	0	Cylindrical, Ø 38 mm	SAZ	Fractured	Fractured
16	30	50	Spherical	HPV-X2	8.4	13.2
17	30	50	Spherical	HPV-X2	7.8	12.7
18	40	50	Spherical	HPV-X2	10.3	16.2
19	60	50	Spherical	HPV-X2	13.3	20.3
20	30	30	Spherical	SAZ	5.6	15.4
21	30	20	Spherical	SAZ	11.1	20.2

3.1.2 | Cylindrical Charge Detonations

The transient out-of-plane displacement contour map of the plate rear surface during the first millisecond of response is shown in Figure 11 for a typical 30 g, 50 mm SOD cylindrical charge. Plates subjected to blast loads arising from cylindrical charge detonations exhibited higher mid-point displacement magnitudes and a greater degree of localisation in the plate profiles when compared to plates loaded from spherical charge detonations of the same SOD and charge mass. This is evident from comparing the sharp deformation peak in Figure 11 (cylindrical charge) to the much flatter, dome-like profile shown in Figure 7 for the equivalent spherical charge.

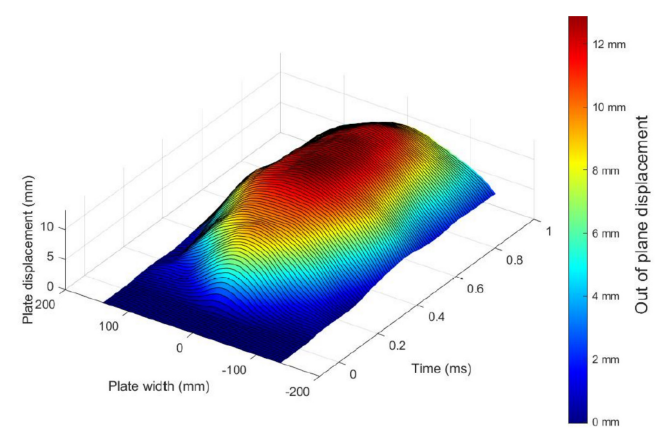


FIGURE 7 | Transient deformation displacement of plate rear surface (30 g detonation, 50 mm SOD, spherical charge test #16).

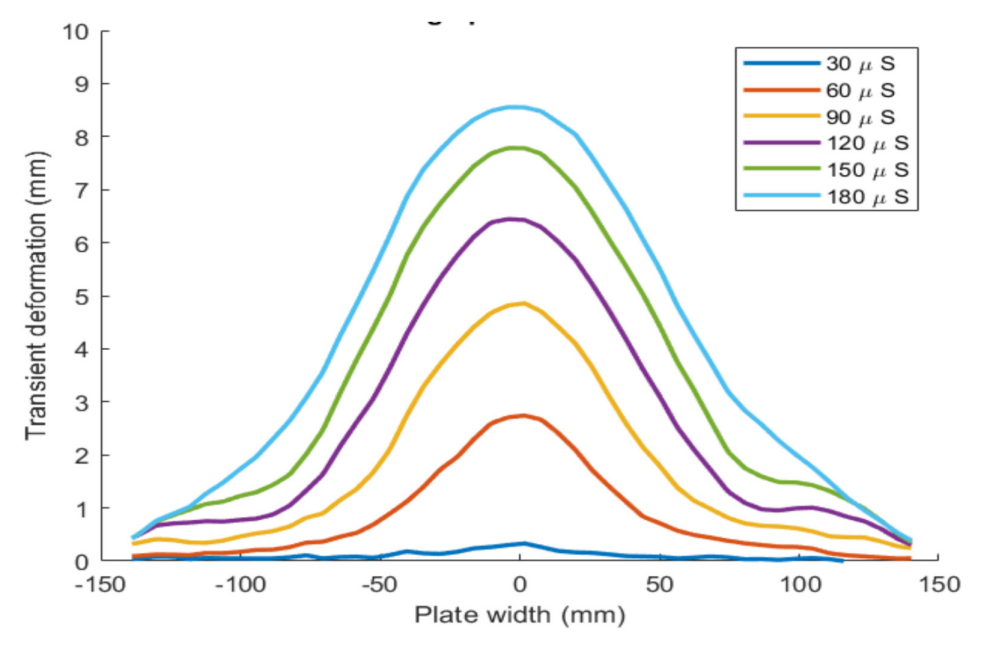


FIGURE 8 | Transient deformation evolution of mid-line profile for a 30 g spherical charge, 50 mm SOD test #17.

The transient mid-line displacement profile of the same plate is shown in Figure 12. The initial deformed profile was localised to the central $100 \, \text{mm}$; as time progresses, the deformation increases in the centre and moves out towards the boundary until the conical type deformed profile extends over the central $200 \, \text{mm}$ wide area after $180 \, \mu \text{s}$.

The inferred out-of-plane velocity distribution across the mid-line for the same test is shown in Figure 13. A high degree of load localisation was clearly visible. The contour plot in Figure 13 shows that, in the early stages of the plate response, velocities were much higher (peaking at 330 m/s) and were applied over a much smaller region than the equivalent spherical test shown in Figure 10. The velocity became even more localised in the tests conducted at closer SODs. In a similar fashion to the spherical plates, but in a more localised band of higher velocities, a dominant plastic shear wave propagated out from the centre towards the boundary. The plate velocity reduced rapidly, and the influence of the boundary on the shear waves was similar to the spherical plates by the time they reached the clamp and reflected back because the plate velocities at that time were similar in magnitude.

The influence of SOD on the mid-point transient displacement history is shown in Figure 14. Figure 14a shows that, as charge mass increased, peak displacement increased as might be expected. The influence of charge mass was similar in Figure 14b,c. The curves in Figure 14 are qualitatively similar, despite the differences in SOD and charge mass. Comparing the curves across Figure 14a-c confirms that plates loaded at closer SODs exhibit higher mid-point displacements for a given charge mass, as expected. The higher velocities and greater degree of localisation in the cylindrical tests account for the 50%–80% larger displacements when compared to their spherical charge counterparts.

Strain, 2025 13 of 28

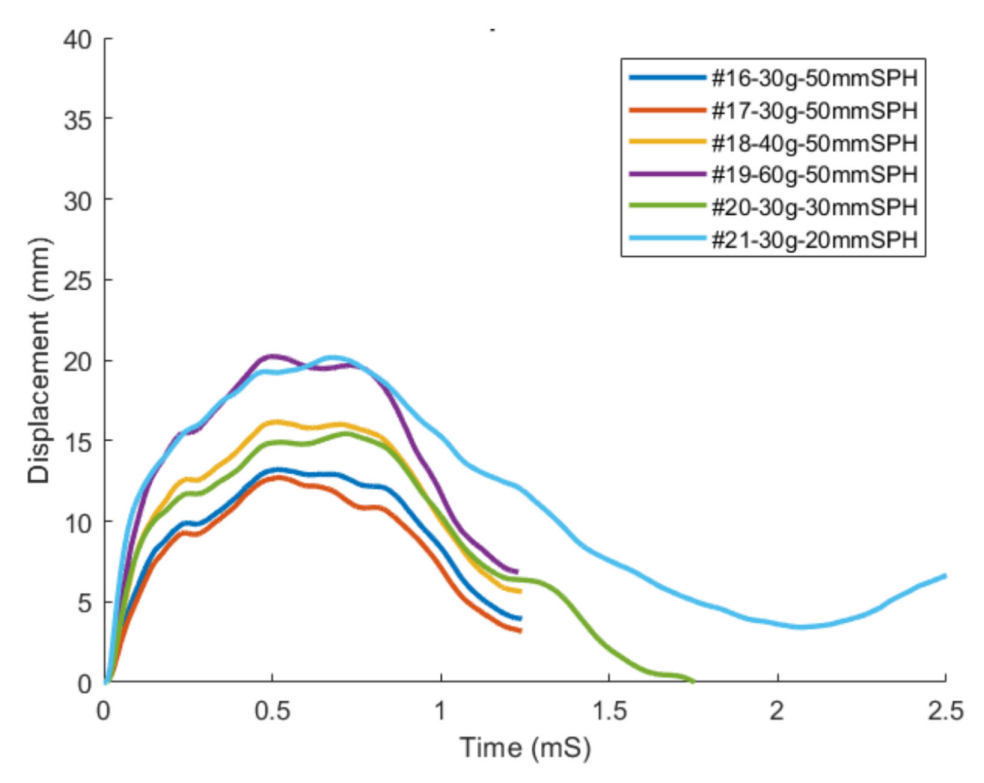


FIGURE 9 | Mid-point displacement–time histories obtained from the spherical charge tests.

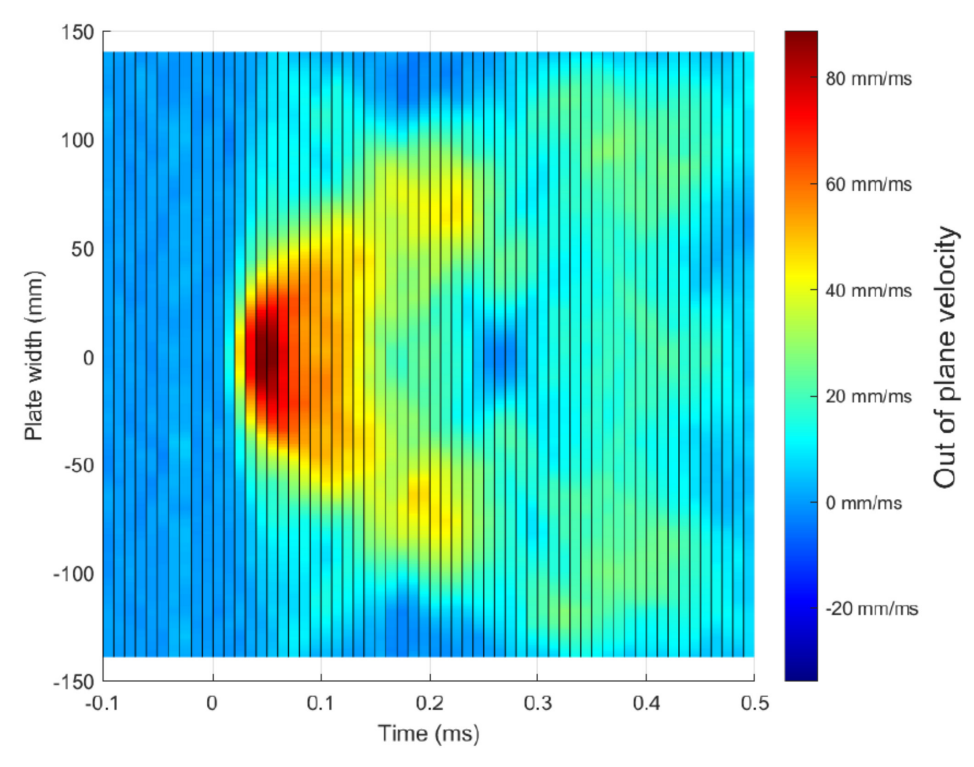


FIGURE 10 | Contour plot showing velocity evolution across the plate during the first 500 μs (30 g detonation, 50 mm SOD, spherical charge test #17).

3.2 | Comparison of Cylinders and Spheres

One of the most interesting comparisons now available is using these full-field data to be able to more accurately compare the resulting deformation of these plates as a result of different loading conditions. This enabled a more accurate evaluation of the asymmetry of the deformation and identification of any modal or shape changes.

14751305, 2025, 6, Downl

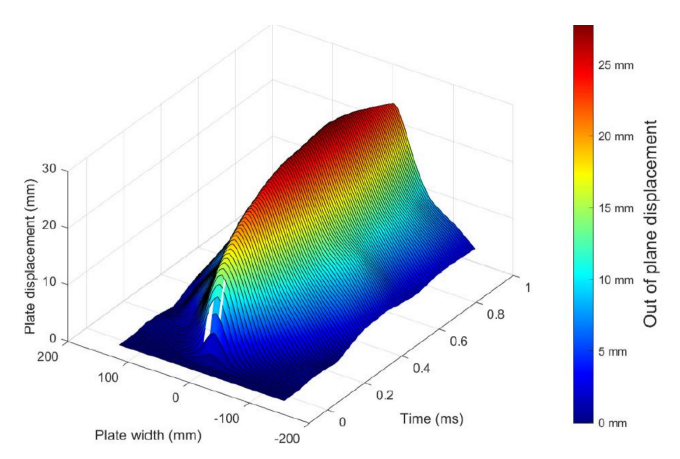


FIGURE 11 | Transient displacement of plate rear surface (30 g detonation, 50 mm SOD, cylindrical) Small areas of data loss indicate decorrelation due to speckle pattern issues.

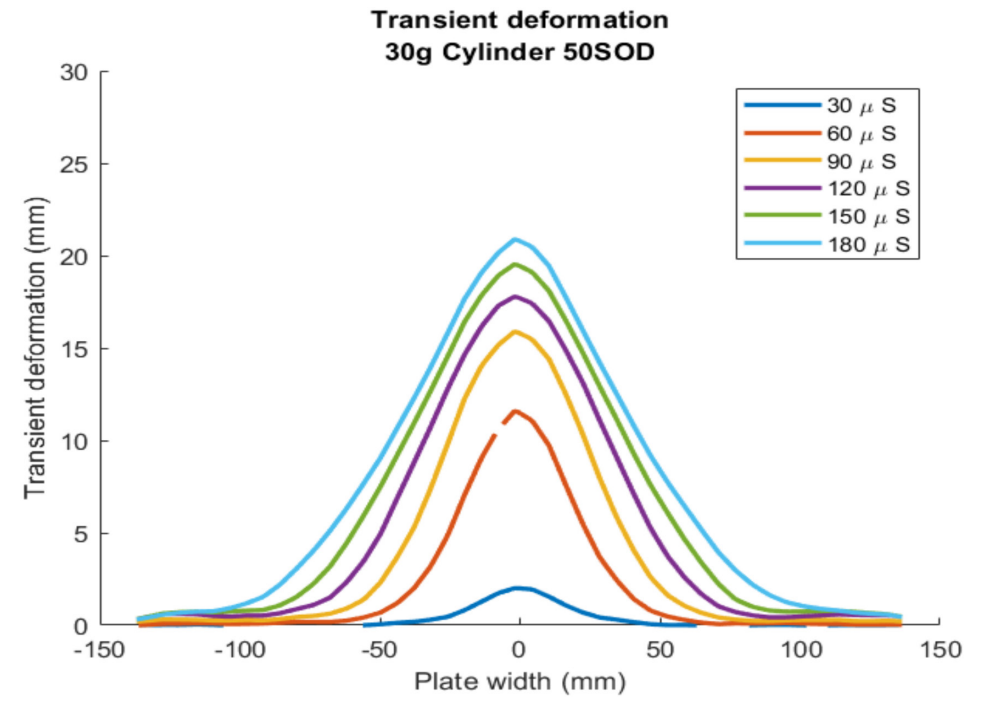


FIGURE 12 | Transient deformation evolution of mid-line profile for a 30 g cylindrical charge, 50 mm SOD.

The resulting displacement fields from tests at different SODs, charge types and masses are shown in Figures 15–17 with the displacements normalised to the maximum peak deflection. When juxtaposed at discrete time intervals, as indicated in Figures 15 and 16, the effects of charge shape on the deformation were evident. At the same SOD, the cylindrical charges caused a more localised and cylindrical deformation profile, contrasted with the much more uniform deformation shape caused by the spherical charges. This strongly correlates to the specific impulse loading, which has been illustrated in Figure 21 for the cylindrical charges and is discussed in more detail in Section 3.4. The transient measurements identified that the boundary condition influenced the shape of the deformation at an earlier time in the spherical charge experiments than that observed in the cylindrical charge detonation tests.

Figure 17 shows the transient response of plates subjected to 20 g cylindrical charge detonations at three different SODs. There was large similarity across the normalised displacement data, illustrating the significant role of charge shape (and its loading) in altering the permanent deformation of a structure when the SOD is kept relatively low. By characterising the transient deformation, we can infer what loading caused it. Having the ability to now consider full-field data (as opposed to single point or line data) on samples at these high frame rates represents a dramatic improvement in the use and evaluation of experimental arrangements used to characterise the deformation and loading of structures exposed to localised blast loading.

Strain, 2025 15 of 28

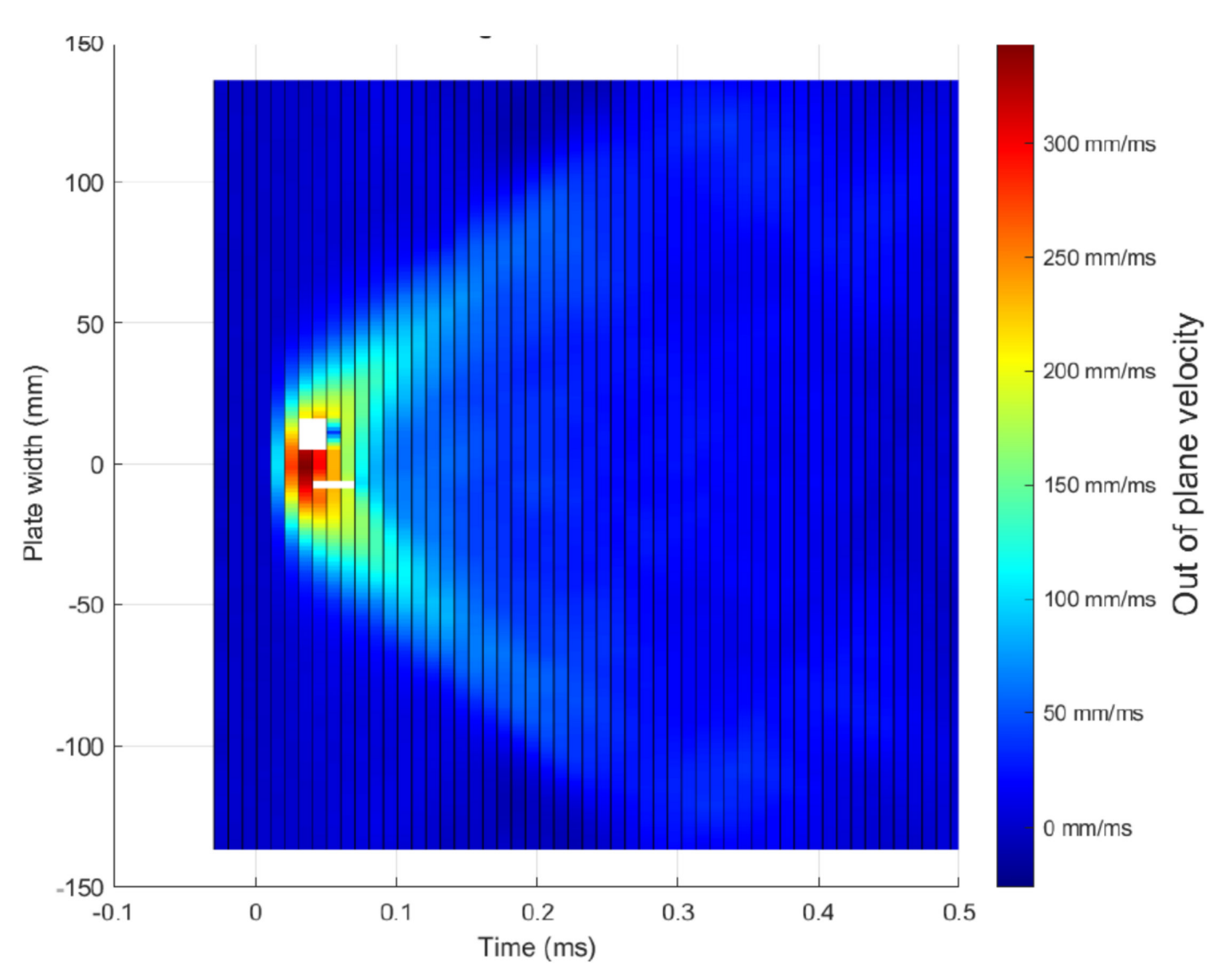


FIGURE 13 | Contour plot showing velocity evolution across the plate during the first 500 µs (30 g detonation, 50 mm SOD, cylindrical charge).

3.3 | Inferring Specific Impulse Distribution

3.3.1 | Method #1: Processed From CoBL Facility Results

The CoBL data was obtained from 10-mm-diameter Hopkinson pressure bars arranged in a cross (with four bars separated at 25 mm increments and a bar at the centre of the cross), providing one pressure measurement at each bar position. This enabled some evaluation of the repeatability at these ordinate measurement points.

When looking at the actual curves produced, there is an initial rise in pressure as the blast wave interacts with the pressure bar. The measurement is averaged over the whole area of the bar face, and each pulse produced is a measure of pressure versus time, which can be integrated to produce a specific impulse measure at each measurement point in space. These measurements run for a long time, meaning that reflections and the propagation of stress waves in the rig appear as pressure readings, so the data curves need to be cropped at a sensible point in time. From numerical models and experiments, it has been shown that loading of the rigid surface should be over in about the first 0.1 ms of the first pressure wave arrival [35], and this is a maximum cut-off point. However, due to the electronics used and the potential interference of the readings from the strain gauges, it is possible that some interference may happen slightly earlier.

In each case, the data was truncated at the same point as the DIC results so that these could be directly compared. An example of this is shown in Figure 18 where the full central bar (X) signal is shown together with the truncation point. Integrating the area under this curve gives us a measure of the specific impulsive loading on the Hopkinson pressure bar, as shown in Figure 3.

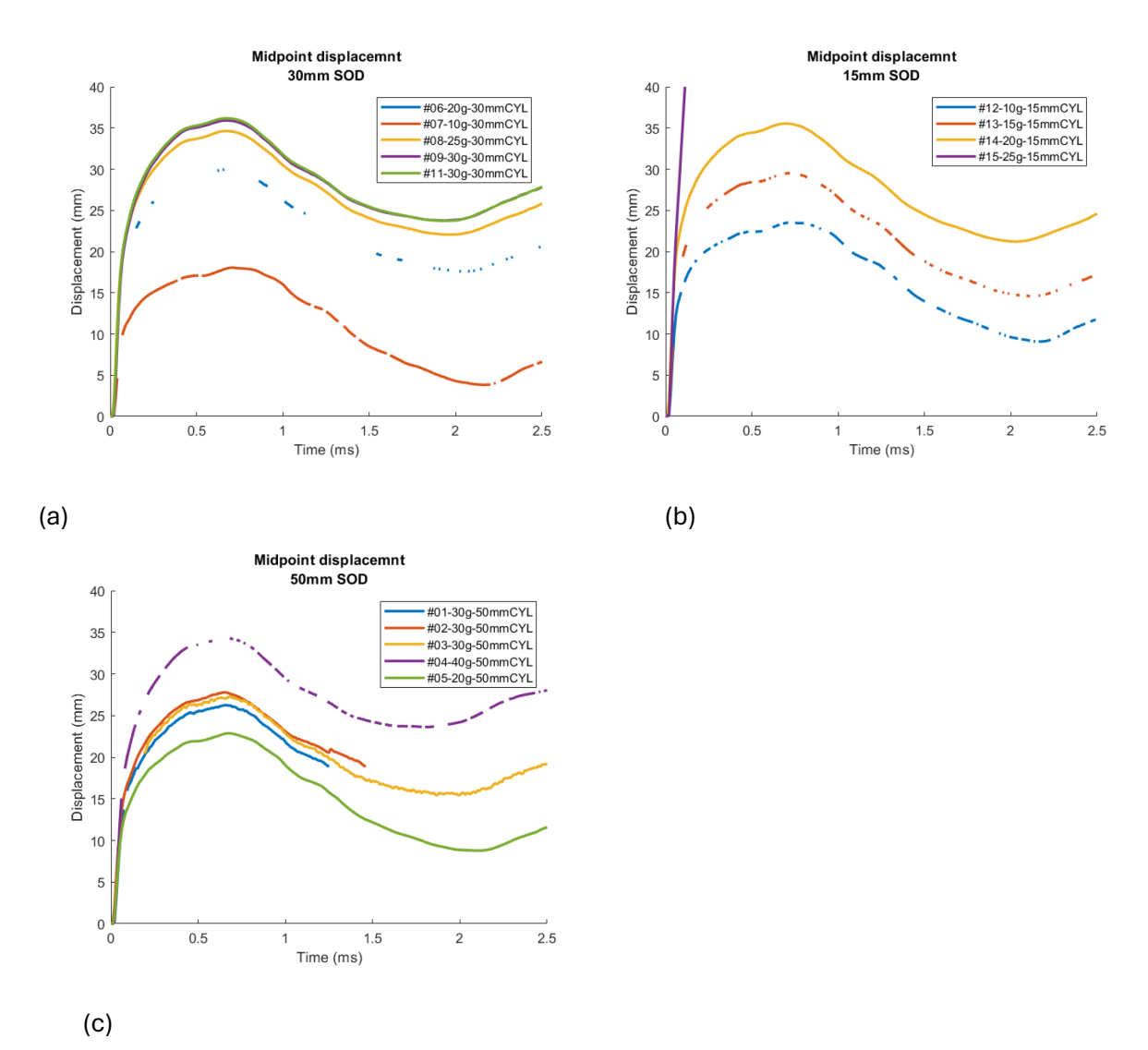


FIGURE 14 | Mid-point displacement-time histories for cylindrical charge detonations at (a) 15 mm SOD (b) 30 mm SOD and (c) 50 mm SOD.

3.3.2 | Method #2: Inferred Using DIC Data

Under impulsive loading conditions, the imparted impulse results in an equivalent change in momentum that can be inferred from the velocity profile of the plate, v(x), using Equation (2). Rigby et al. [16] used this approach to infer impulse from similar localised blast loading experiments, albeit at slower frame rates with a limitation of only getting a single velocity data point. The specific impulse was calculated and compared with impulses obtained from CoBL at a larger scale, showing favourable agreement using scaled data.

$$i(x) = \rho t. v(x) \tag{2}$$

where i(x) is the specific impulse, ρ is the density (assumed to be $7850 \,\mathrm{kg/m^3}$) and t is the plate thickness (nominally 3 mm, but the measured value is used for each test).

This current work offers the opportunity for a similar comparison of maximum specific impulse at higher frame rates and thereby a better temporally and spatially resolved velocity field, without the need to scale the CoBL data. From the velocity field data shown in Figures 10 and 13, it is evident that the velocity field evolved both spatially and temporally, so determining the velocity field v(x) across an appropriate time period was essential. In other words, a robust method for selecting the magnitude of v(x) at each location of x was needed to obtain the maximum applied impulse but does not include features of the velocity field that evolve later due to features of the structural response.

The experimental data showed that, as the initial disturbance of the pressure wave acting on the centre of the plate began to move the plate, a strain wave propagated outwards from the plate centre towards the clamped boundary. As this wave reached the boundary, a reaction wave propagated back towards the plate centre. This is more evident in Figure 19, which plots the out-of-plane velocity of a

Strain, 2025 17 of 28

Displacement comparison of 30g Charges 30mm SOD

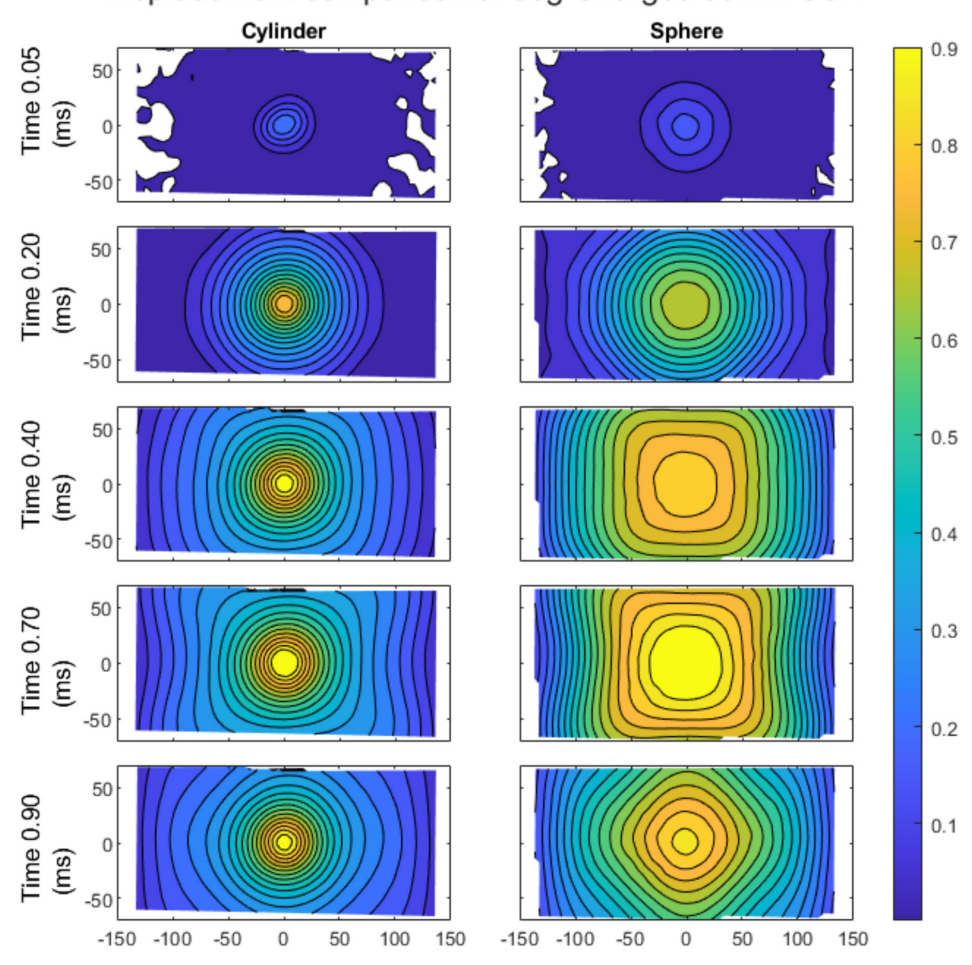


FIGURE 15 | Comparison of the 30 g cylindrical (left) and spherical (right) charges at a SOD of 30 mm illustrating the normalised evolution of the out-of-plane deformation shapes of the plates.

plate from a 30 g spherical charge test (#20). As the centre of the plate was still deforming ($60\,\mu s$ after detonation), a strain wave initiated and began moving inwards from the clamped boundary towards the centre. This phenomenon was expected in plates exhibiting large deflections but can interfere with the specific impulse inferred from the plate velocity by artificially adding impulse into the relatively simple calculation.

The time that this wave initiated at the boundary and propagated towards the plate centre coincided with the time it would take a wave to move from the centre to the boundary (estimated using the wave speed of steel and the 100-mm linear distance of plate). It is recommended that, when using DIC to infer impulse from the plate velocity, the data are checked for the presence of these strain waves and that if they are present, the time over which the specific impulse is estimated should not exceed the temporal limit of the wave speed distance of the plate.

3.3.3 | Specific Impulse Distribution Results

Specific impulse distributions inferred using the DIC method were compared to impulse distributions obtained from CoBL pressure bar data at discrete bar locations. Figure 20 shows the maximum specific impulse distribution across the plate midline for the DIC approach and the equivalent CoBL test, from a 20 g detonation at 50 mm SOD. The error bars in the dashed CoBL line at 25 mm increments indicate the variation from average specific impulse calculated from four bars at that radial ordinate. The variation in CoBL impulse is not large enough to account for the difference between the CoBL and DIC specific impulse peak at the centre. When the resulting specific impulse is compared in Figure 20, we can see that close agreement in the overall shape is observed, with a small underestimation of the DIC inferred impulse reported in the central 50 mm. A similar result was obtained for other charge masses, illustrated by the plot in Figure 21 for the 30 g test. Three DIC tests were performed at 30 g and show good repeatability of the DIC method with itself. The central specific impulse peaks are consistently lower than the CoBL data.

Displacement comparison of 30g Charges 50mm SOD

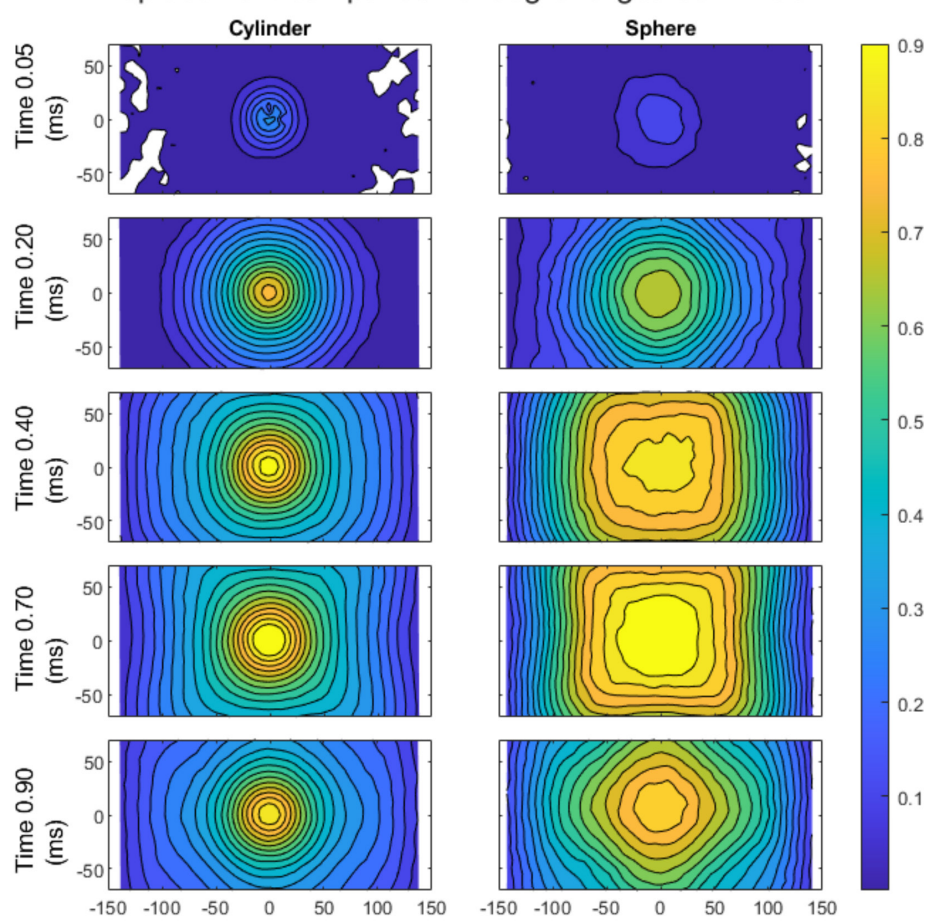


FIGURE 16 Comparison of the 30g cylindrical (left) and spherical (right) charges at a SOD of 50 mm illustrating the normalised evolution of the out-of-plane deformation shapes of the plates.

The overall results indicate that, in general, the maximum inferred DIC specific impulses at the plate centre were 0.35 MPa.ms (30 g cylinders) and 0.15 MPa.ms (20 g cylinders) lower than those found using CoBL. This difference is very small, between 2% and 5%. Rigby et al. [13] proposed that the DIC approach might exhibit this feature due to the inertia or shear resistance of the plates. However, shear resistance should have a negligible role for plates with such a small thickness/length ratio [41].

The shape of the specific impulse distribution results for the 20 and 30 g cylindrical detonations at 50 mm SOD are shown in Figures 20 and 21, respectively. The DIC results compare very well to the CoBL tests over the measured area of interest. There are slight differences present in the two measurement techniques, but these are well within the normal experimental variation seen in the literature for cylindrical charge loading work. This small difference could be attributed to either FSI or the plate response slightly smearing the impulse imparted over a larger area (and being more affected by the plate boundary response in the deformable plate experiments).

Accepting that the specific impulse inferred from DIC is a good approximation, this information was used to better understand the much finer spatial and temporal data over the plates. Figure 22 shows the specific impulse distribution from 30 g charges at a 50 mm SOD, but for spherical- and cylindrical-shaped charges. The impulses were higher in the central region for the cylindrical charge detonation. There was a similar loading wave that moved from the centre of the plate towards the clamp boundary in both loading cases.

In the spherical charge detonations, the impulse profile was more rounded (i.e., more distributed central loading) compared to the cylindrical charge. There was a more visible wave moving from the clamp boundary towards the plate centre for the spherical charge. This is significant, as if any of this reported loading is due to a boundary effect then it would result in an artificial impulse being added to the global impulse estimate.

Strain, 2025 19 of 28

Displacement comparison of 20g Cylinders

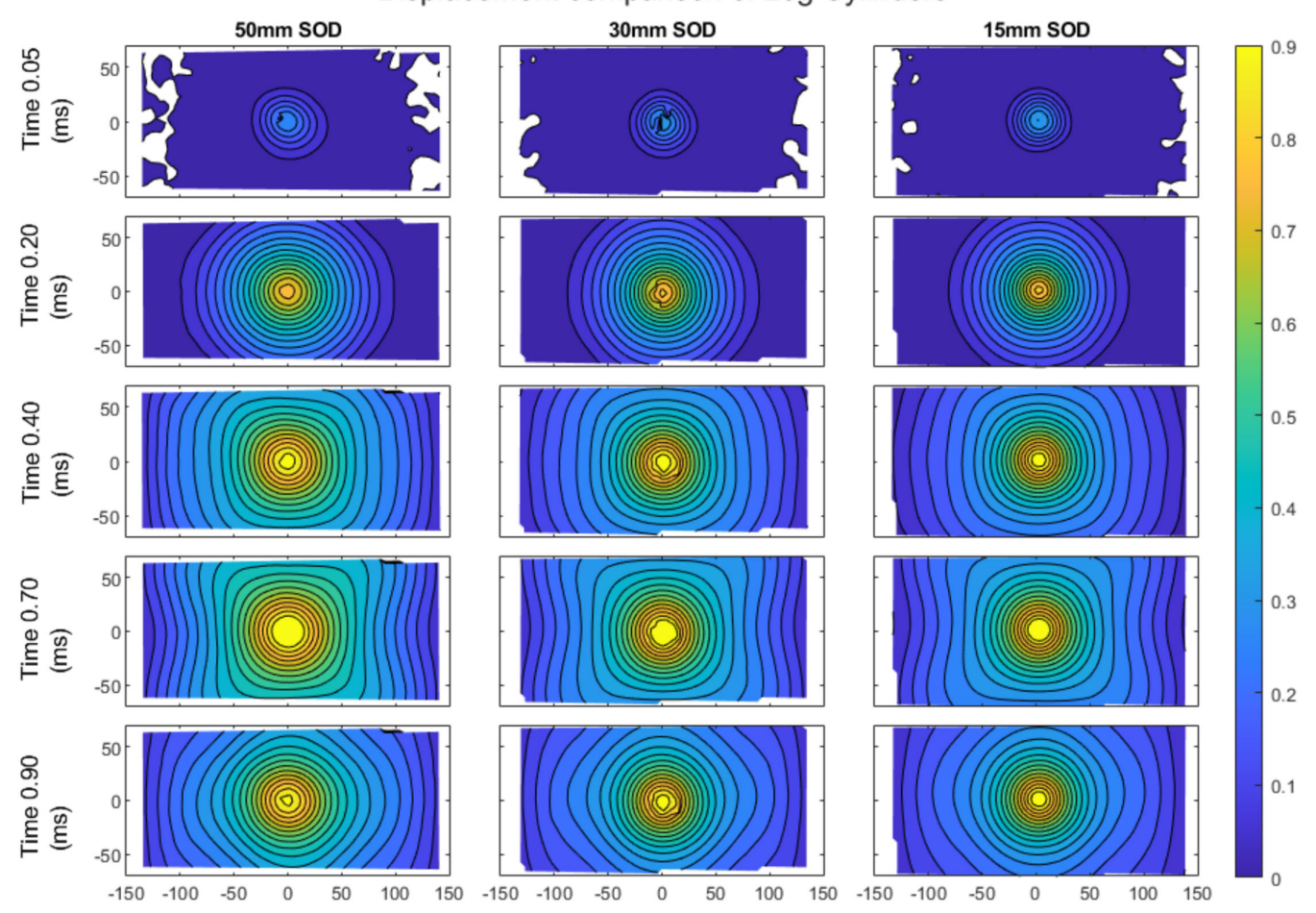


FIGURE 17 | Comparison of the cylindrical charges at varying SOD of 50 mm (left), 30 mm (middle) and 15 mm (right) illustrating the normalised evolution of the out-of-plane deformation shapes of the plates to illustrate the effect of loading localisation on the deformation shape.

By drawing an analogy between conventional instrumentation (such as a Hopkinson bar) and inferring impulse from DIC plates, this phenomenon could be viewed as a signal spike that obscures the true measurement, limiting the time over which the instrument is considered reliable. In this work, the data were truncated after this point, similar to the truncation of Hopkinson bar signals after times when wave reflections are expected to interfere. To overcome this possible limitation over which DIC can be accurately used to infer impulse, a larger span plate could be used—this would increase the time taken for the waves travelling through the steel plate to reach the boundary and reflect back, increasing the 'recording time' of the plate as an effective specific impulse measuring instrument. A similar idea is behind the design of longer Hopkinson bar systems for increasing the useful test duration.

3.4 | Fragment Velocity

The 25g cylindrical detonation at 15 mm SOD resulted in capping failure of the plate, with a circular fragment ejected from the plate centre. The sequence of images shown in Figure 23 shows the plate deformation in its early stages at the plate centre (Figure 23a) and the highly localised deformation band forming at the cap diameter (Figure 23b). After $60\mu s$, a cap was ejected from the plate (Figure 23d).

As the speckle pattern and the cap remain intact during the deformation and failure process, it was possible to use subsequent frames, $10\,\mu s$ apart, to estimate the plate and cap velocity over the first $150\,\mu s$. The transient velocity profiles across the plate midline at several times prior to plate fracture are shown in Figure 24a. The plate velocity was highly localised and reached a peak of $600\,m/s$ prior to fracture after $50\,\mu s$ before decreasing as the velocity wave started to propagate radially across the plate. However, the high central velocities caused rapid deformation and subsequent failure localisation. The fracture process caused the cap velocity to decrease once it was fully detached from the main plate, as some of the kinetic energy was converted to strain energy during fragmentation. The 'noisy' velocity profile (at $80\,\mu s$) indicates the final detachment of the cap from the plate. The evolution of the cap velocity is shown in Figure 24b and gives an estimated constant residual velocity of $346\,m/s$ (averaged between 80 and $150\,\mu s$). This is similar in magnitude to the cap fragment velocities of blast loaded steel plates estimated from PE4 detonations on mild steel plates. Wiehahn et al.



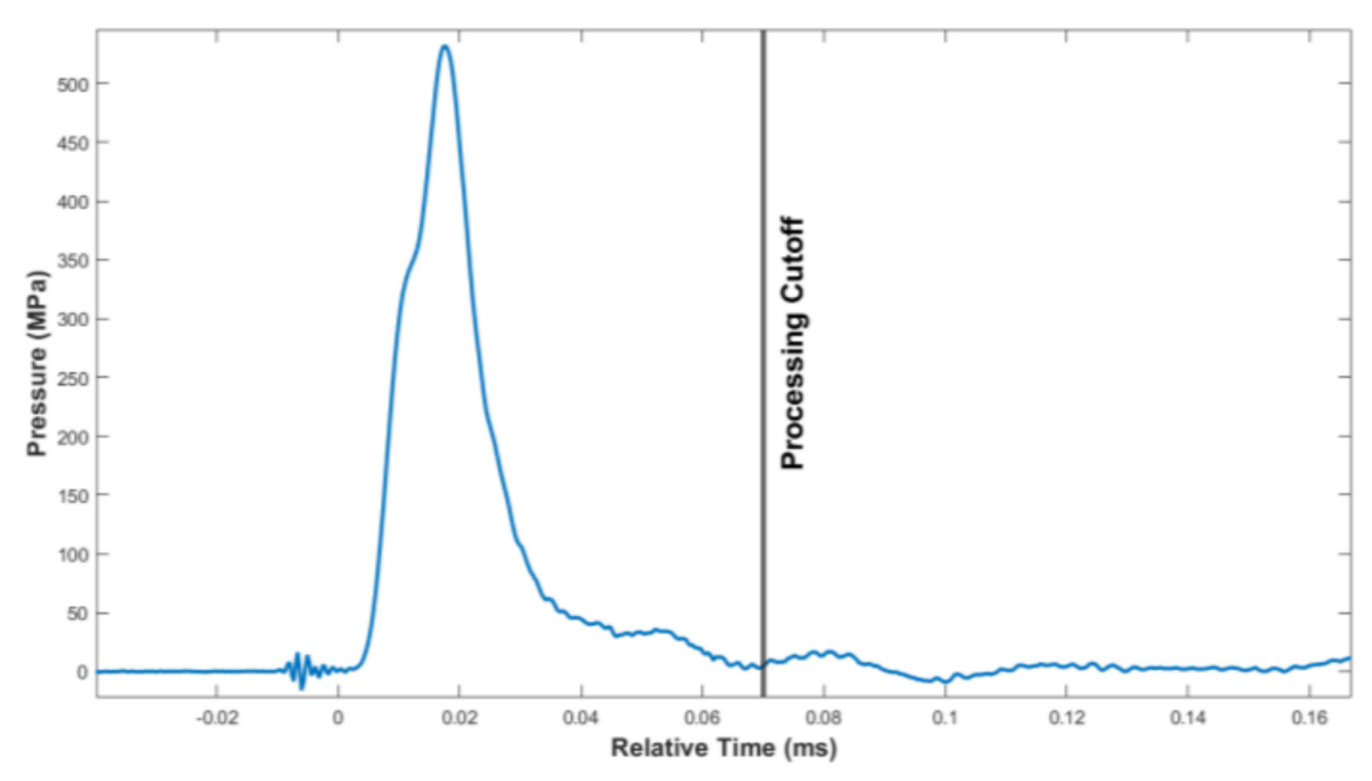


FIGURE 18 | The typical point in time where the Hopkinson bar pressure signals are cropped for processing about 70 μ s after the initial pressure rise on the central bar.

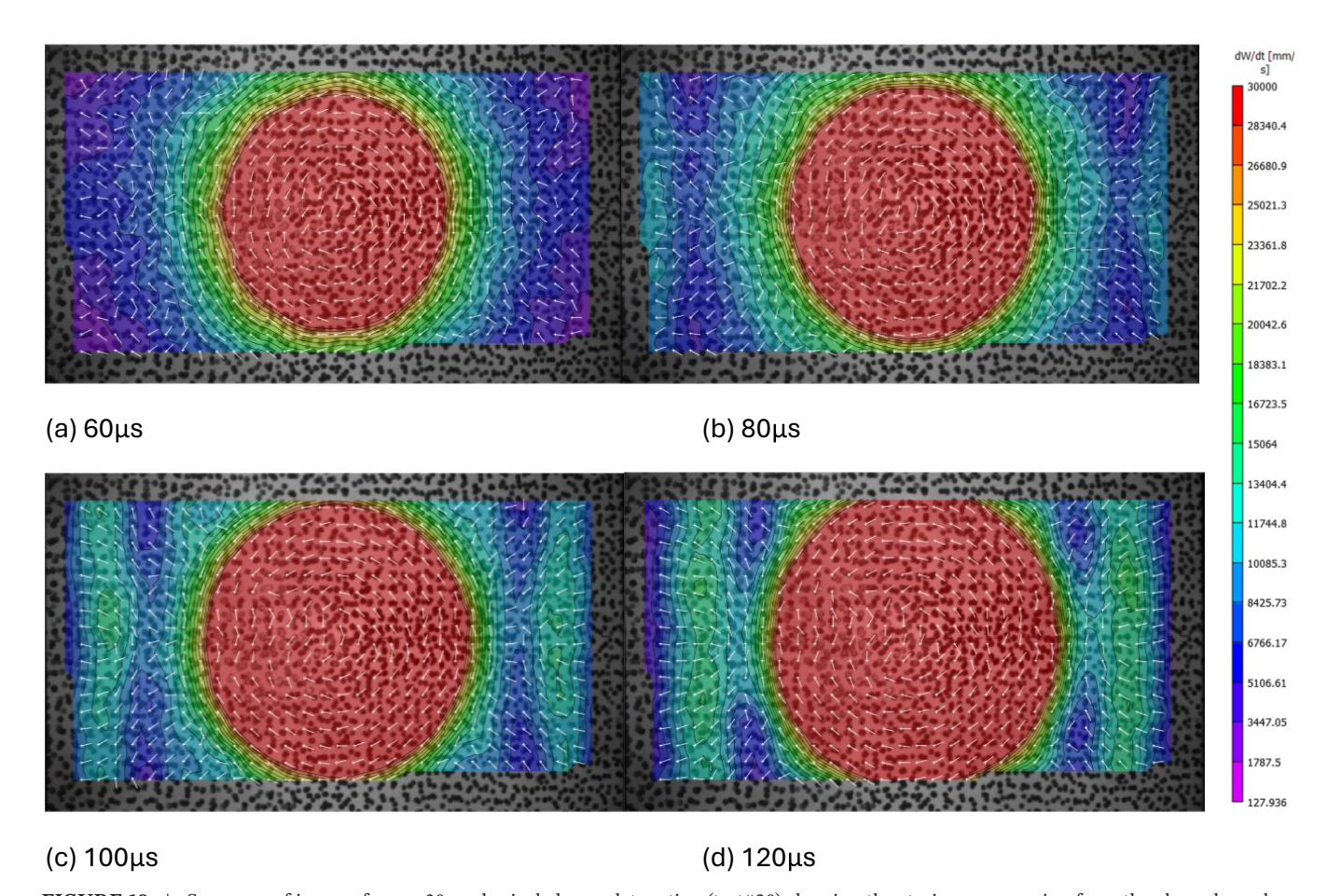


FIGURE 19 | Sequence of images from a 30 g spherical charge detonation (test#20) showing the strain wave moving from the clamp boundary back towards the plate centre at different time points after detonation: (a) $60 \,\mu s$, (b) $80 \,\mu s$, (c) $100 \,\mu s$ and (d) $120 \,\mu s$.

Strain, 2025 21 of 28

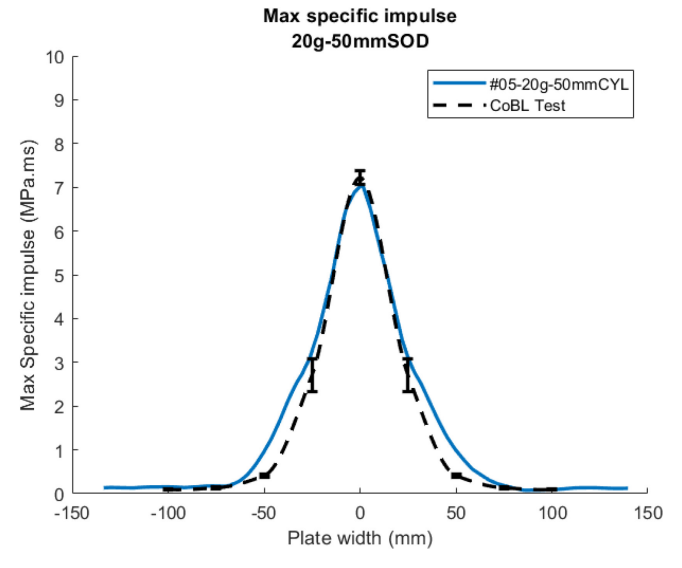


FIGURE 20 | Specific impulse distribution results for 20g cylindrical charge at 50 mm SOD.

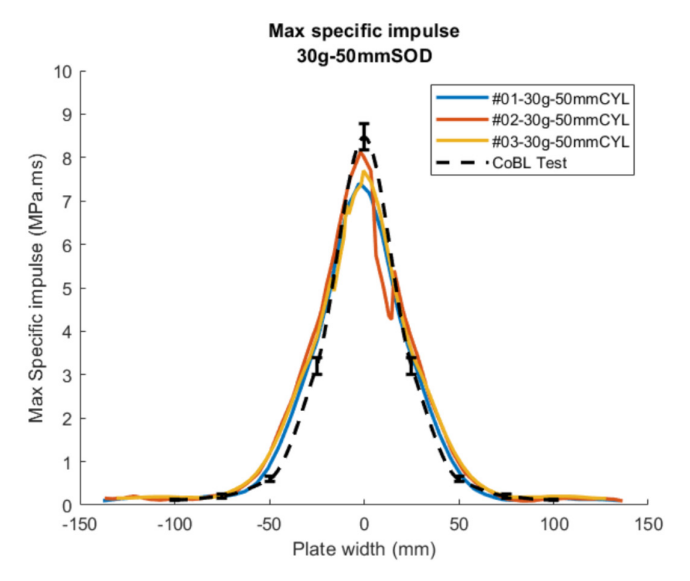


FIGURE 21 | Specific impulse distribution results for 30 g cylindrical charge at 50 mm SOD.

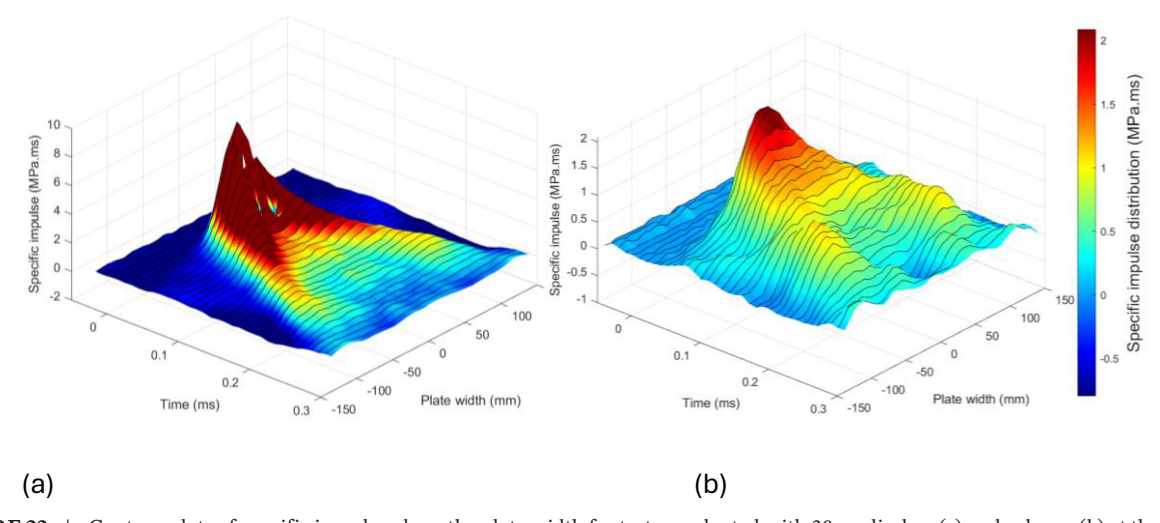


FIGURE 22 | Contour plots of specific impulse along the plate width for tests conducted with 30 g cylinders (a) and spheres (b) at the same SOD of 50 mm (the colour map has been adjusted in the images so pressures above 2 MPa.ms are shown in the same colours).

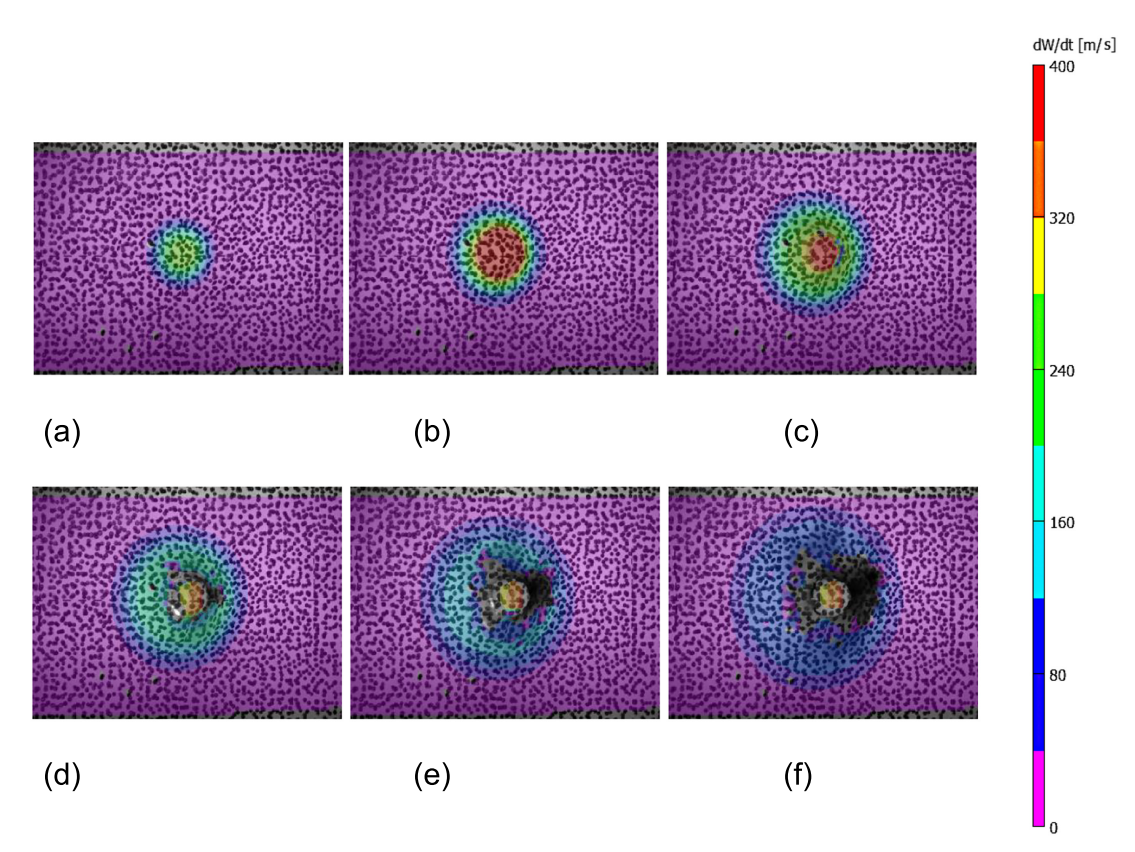


FIGURE 23 | Sequence of images showing (a) initial plate deformation at 20 μs, (b) 40 μs, (c) 60 μs, (d) 80 μs, (e) 100 μs and (f) 120 μs.

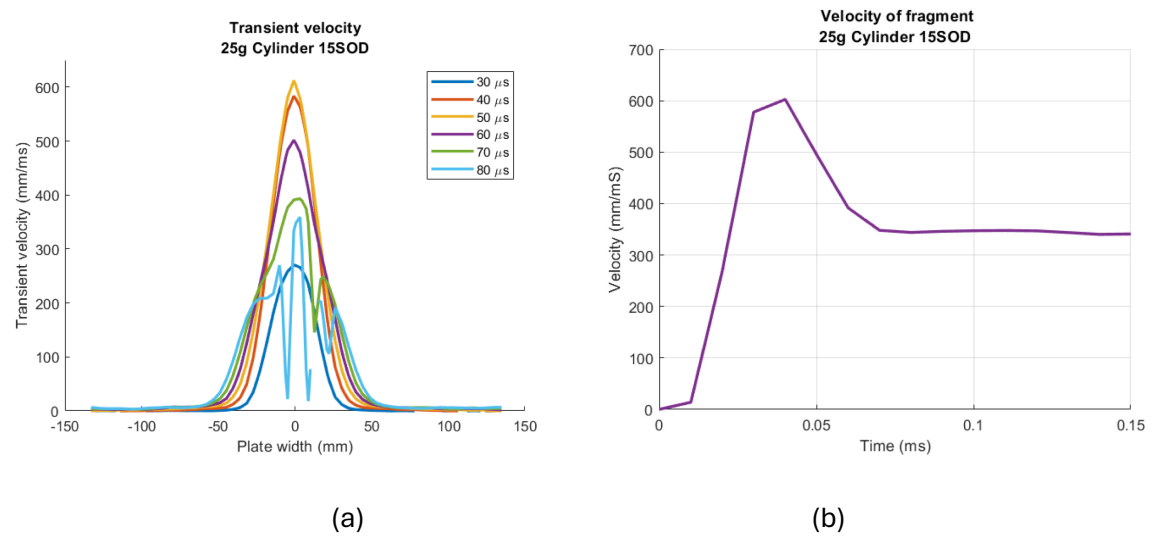


FIGURE 24 | Transient velocity measurements. (a) Mid-line profile during the first 80 µs. (b) Velocity of plate centre (cap location) versus time.

[42] observed cap fragments from locally blast loaded plates of 294 m/s, whereas Nurick et al. [43] measured velocities ranging from 52 m/s (11.5 g PE4) to 378 m/s (24.1 g PE4). Fragment velocity varies according to charge mass and configuration, material density and specimen thickness.

3.5 | Initial Thoughts on the Uptake of Specific Impulse

The spatial and temporal resolution of the DIC records suggests the possibility of a detailed assessment of how the loading is taken up by the target plate in the early stages and the degree to which the DIC data can be interpreted to give an assessment of the loading itself. This issue requires more attention than can be provided here and will be addressed in detail in future articles. However, some initial thoughts are presented here.

Strain, 2025 23 of 28

Rigby et al. [13] first noted the correlation between CoBL direct impulse measurements and the local momentum observed in the early stages of DIC records of plate response to similar loading. That was predicated on assumptions of perfectly impulsive loading conditions: The impulse is applied over a timescale where the structural deformation of the target plate is insignificant. However, the results presented here suggest a more complex reality. Figure 3 shows load durations as measured by the CoBL rig of around $50\,\mu s$. Figure 12 shows that by that time after the onset of loading, there is a highly localised plate response, with an epicentral deformation of several plate thicknesses and little or no deformation at radial offsets greater than $50-60\,m s$. This implies the existence of very high shear and/or membrane strains, implying the likelihood of a mechanism whereby the impulse imparted to the centre of the plate will be distributed to some degree to more peripheral regions while the loading is still being applied. This impulse effect can be seen by looking at the cross-sectional velocity profiles illustrated in Figure 25 where these effects become more apparent around the $50-60\,m s$ radial distance.

In these circumstances, we might expect the maximum momentum which the central region of the plate experienced to be somewhat lower than the impulse recorded in CoBL tests, whereas at some peripheral regions, the peak momentum might be a combination of the actual applied load and momentum transferred from the highly deformed central region.

Specific impulse distribution with radial offset data shown in Figure 26a broadly shows that pattern. The epicentral maximum momentum observed in the DIC test is somewhat lower than the central specific impulse measured directly in the CoBL tests (with the caveat that the 0 mm radial offset CoBL data comes from just 1 bar and may be affected by local structures in the fireball), whereas at radial offsets between approximately 20 and 60 mm, peak momentum recorded on the deforming plate is somewhat higher than the directly measured specific impulse. At greater radial offsets, the DIC peak momentum is a little lower than the CoBL specific impulse, suggesting another momentum transfer mechanism.

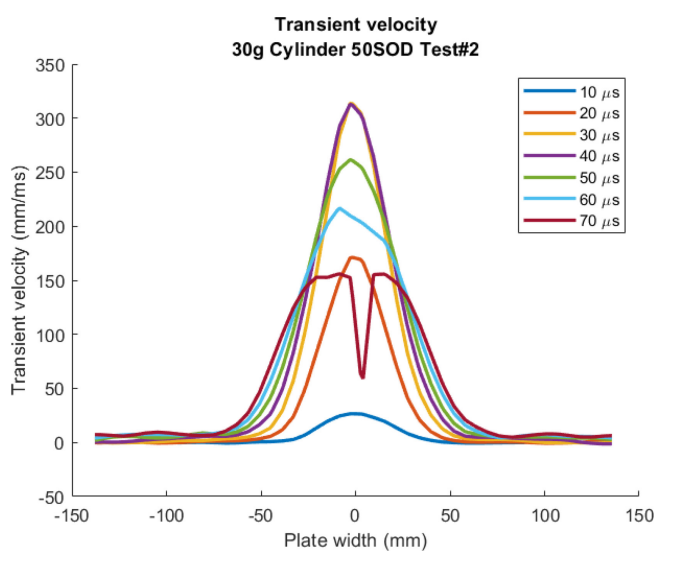


FIGURE 25 | Transient velocity profiles of the central cross section for test #2, 30 g charge detonation at 50 mm SOD.

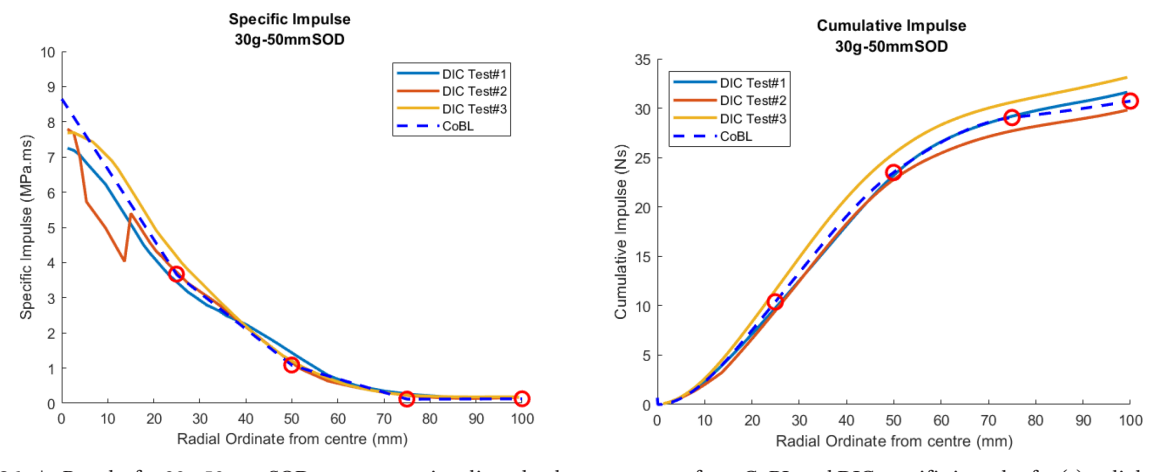


FIGURE 26 | Results for 30 g 50 mm SOD tests comparing direct load measurement from CoBL and DIC specific impulse for (a) radial distribution of observed specific impulse/momentum and (b) cumulative total impulse against integration radius from spatial integration (red circles indicate CoBL data points).

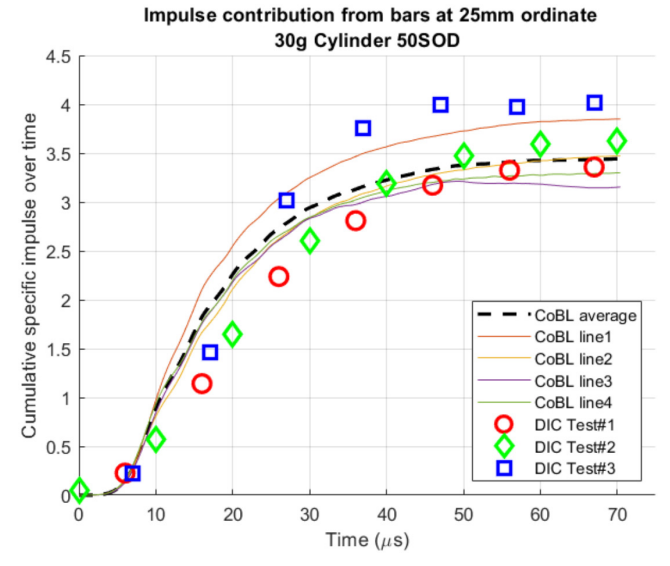


FIGURE 27 | Results for 30 g 50 mm SOD tests showing how the cumulative specific impulse is evaluated at a 25 mm ordinate for both test methods (symbols placed at DIC temporal measurement points).

Figure 26b shows how these specific impulse/momentum data integrate into cumulative N.s impulse as we extend the radius of integration. This approach essentially shows the same data as Figure 26a but accounts for the increased area over which the values at larger radial offsets are applied. The total impulse magnitude and distribution obtained by the two methods are broadly similar, although the precise magnitudes and derivatives vary slightly.

This analysis suggests that the prize of being able, non-invasively, to extract accurate spatial maps of the loading imparted to a deformable plate, in addition to the deformation maps, is within reach. It appears possible to extract the broad form of spatial distribution of impulse applied to the plate. Consideration of momentum transfer mechanisms in early-stage deformation may further refine the potential to extract loading data and is currently under investigation by the authors.

Ultimately, by applying this method with an increased temporal resolution, this indicates that we are finally able to reliably predict the temporal and spatial data for these tests in a non-invasive way, which represents a massive increase in the spatial resolution that could be achieved. We are able to move from individual discrete data points where Hopkinson pressure bars have been placed to full-field information, provided it can be imaged by the camera system. It should be noted that there is some trade-off in temporal resolution at each point which can be seen in Figure 27 (which would be increased by increasing the camera frame rate), but this is outweighed by the increase in spatial resolution that can be achieved using this method seen in Figure 26. The results achieved and illustrated in Figure 27 for the 25 mm radial ordinate where data for CoBL can be directly compared to that of DIC indicate the potential for this method to impact the future of this experimental testing, producing a rich dataset that can be used to better uncover the loading being applied to these structures in a highly dynamic and extremely challenging environment.

4 | Conclusions

There are many complexities to using high/ultra-high-speed camera technology in blast testing. In addition to the previously highlighted issues of the short duration and high magnitude pressure pulse loading, high temperature fireball and the light flash emitted by detonation, this work addressed issues that have not previously been discussed, namely, appropriate sizing of the plate, uncertainty in the post-processed measurements and the possible dependence on camera system in obtaining full-field data in the first $100\,\mu s$ of response. The results presented in this study illustrate the groundbreaking potential of ultra-high-speed imaging, combined with careful application of DIC, to measure the full-field transient displacement and velocity fields of a blast-loaded structure. This means that both the impulsive loading and structural response can be obtained from non-contact imaging techniques across a visible plate surface. This data can be used to extract the full spatio-temporal impulse loadings, which are inherently driven by the pressure of the blast loading.

The accuracy of two different commercial camera systems was found to be comparable for this application (with very low uncertainties and system-related errors), although the higher resolution camera sensor produced lower noise DIC results. The slight improvement is attributed to a combination of sensor bit rate, resolution and pixel size. However, for practical purposes, the differences were insignificant compared to the variation in transient deformation expected from test to test.

Specific impulse distributions in the full field from DIC were compared to Hopkinson pressure bar measurements from CoBL test data that were post-processed to produce impulses at discrete locations. Interrogation of the results showed that, when a specific

Strain, 2025 25 of 28

impulse was localized at a point in the structure (in this case, the plate centre), the resolution of the DIC method will be sensitive to the plate thickness because of the shear resistance and inertia it offers, whereas CoBL test data are sensitive to the position and diameter of the bars. Boundary strain waves were shown to potentially obscure the specific impulse being inferred unless appropriate post-processing was utilised—in this case, time cropping. Thus, provided shear effects do not dominate response and any interference from wave reflections at the boundary is accounted for (and do not arrive at times when the loading impulse is still present), the DIC approach provides reliable and accurate estimates of the impulse distribution across a blast loaded plate.

The design of the DIC blast plate arrangement can be understood through analogy with standard instrumentation. For example, the test plate design can be modified to minimise the influence of wave reflections and improve the resolution of localised impulses and deformations. Increasing the plate span increases the time available to 'record' the loading impulse before structural response waves arrive in the region of interest. Using a plate that is as thin as possible (without rupturing) will improve the resolution of localised impulse distributions by reducing shear resistance (and 'smoothing' of the impulse). However, there is a trade-off similar to that of using a correctly sized load cell: reducing plate thickness leads to increased initial plate velocities, raising the possibility of motion blurring of the images if the exposure time is not kept sufficiently short and/or the lighting is inadequate.

For the first time, this work has shown that it is also possible to measure the velocity of a ruptured fragment from a blast-loaded plate without the combustion products and residual pressure obscuring the measurements or damaging the camera system using DIC. The rupture limit of Strenx700 plates was found to be 25 g for a 38 mm cylindrical charge placed at a 15 mm SOD. The failure of the plate and fragment velocity was evaluated through a combination of velocity fields inferred using DIC and a visual inspection of the camera footage. A maximum velocity of 600 m/s immediately prior to fracture and a residual flight speed of the fragment at almost 350 m/s were measured, with the difference attributed to the energy used in the fracture process during the detachment of the fragment from the main plate.

This novel application of DIC to full-field impulse determination and residual fragment velocity measurements, along with rigorous error evaluation, represents a step change in the validation of load and response of near-field blast-loaded plates that will prove invaluable to blast engineers and model developers.

Author Contributions

R. J. Curry: conceptualization, methodology, software, data curation, investigation, validation, formal analysis, project administration, writing – original draft, writing – review and editing. **G. S. Langdon:** conceptualization, writing – original draft, writing – review and editing, project administration, resources, supervision. **A. Tyas:** writing – review and editing, resources, funding acquisition, supervision.

Acknowledgements

The authors acknowledge the support of the EPSRC fund EP/V007637/1 for Blast and Impact diagnostics laboratory. The authors also acknowledge the invaluable contribution of the technicians at the University of Sheffield Blast laboratory, with special thanks to Mr Andy Hibbert for his expertise and assistance with the camera systems. The authors also acknowledge the support and assistance from Dr John Philip Tyler and Correlated Solutions for enabling correct installation and operation of the camera systems and post-processing using VIC-3D. The authors wish to acknowledge the very useful questions raised and conversations with Dr Fabrice Pierron and the British Society for Strain Measurement.

Conflicts of Interest

The authors declare no conflicts of interest.

Data Availability Statement

The data that support the findings of this study are available on request from the corresponding author. The data are not publicly available due to privacy or ethical restrictions.

References

- 1. H. L. Brode, "Numerical Solutions of Spherical Blast Waves," Journal of Applied Physics 26, no. 6 (1955): 766-775, https://doi.org/10.1063/1.1722085.
- 2. C. N. Kingery and G. Bulmash, "Air Blast Parameters From TNT Spherical Air Burst and Hemispherical Surface Burst," ARBRL-TR-02555 Report, (1984).
- 3. S. E. Rigby, A. Tyas, T. Bennett, S. D. Fay, S. D. Clarke, and J. A. Warren, "A Numerical Investigation of Blast Loading and Clearing on Small Targets," *International Journal of Protective Structures* 5, no. 3 (2014): 253–274, https://doi.org/10.1260/2041-4196.5.3.253.
- 4. S. E. Rigby, C. Osborne, G. S. Langdon, S. B. Cooke, and D. J. Pope, "Spherical Equivalence of Cylindrical Explosives: Effect of Charge Shape on Deflection of Blast-Loaded Plates," *International Journal of Impact Engineering* 155 (2021): 103892, https://doi.org/10.1016/j.ijimpeng.2021.103892.
- 5. S. E. Rigby, A. Tyas, and T. Bennett, "Single-Degree-of-Freedom Response of Finite Targets Subjected to Blast Loading The Influence of Clearing," *Engineering Structures* 45 (2012): 396–404, https://doi.org/10.1016/j.engstruct.2012.06.034.

- 6. C. Langran-Wheeler, S. E. Rigby, S. D. Clarke, A. Tyas, C. Stephens, and R. Walker, "Near-Field Spatial and Temporal Blast Pressure Distributions From Non-Spherical Charges: Horizontally-Aligned Cylinders," *International Journal of Protective Structures* 12, no. 4 (2021): 492–516, https://doi.org/10.1177/20414196211013443.
- 7. O. G. Alshammari, O. S. Isaac, S. D. Clarke, and S. E. Rigby, "Mitigation of Blast Loading Through Blast-Obstacle Interaction," *International Journal of Protective Structures* 14, no. 3 (2023): 357–389, https://doi.org/10.1177/20414196221115869.
- 8. G. Valsamos, F. Casadei, G. Solomos, and M. Larcher, "Risk Assessment of Blast Events in a Transport Infrastructure by Fluid-Structure Interaction Analysis," *Safety Science* 118 (2019): 887–897, https://doi.org/10.1016/j.ssci.2019.06.014.
- 9. C. Fallon and G. J. McShane, "Fluid-Structure Interactions for the Air Blast Loading of Elastomer-Coated Concrete," *International Journal of Solids and Structures* 168 (2019): 138–152, https://doi.org/10.1016/j.ijsolstr.2019.03.017.
- 10. S. D. Clarke, S. D. Fay, J. A. Warren, A. Tyas, S. E. Rigby, and I. Elgy, "A Large Scale Experimental Approach to the Measurement of Spatially and Temporally Localised Loading From the Detonation of Shallow-Buried Explosives," *Measurement Science and Technology* 26, no. 1 (2014): 015001, https://doi.org/10.1088/0957-0233/26/1/015001.
- 11. S. D. Clarke, S. E. Rigby, S. D. Fay, et al., "Characterisation of Buried Blast Loading," *Proceedings of the Royal Society A* 476 (2020): 20190791, https://doi.org/10.1098/rspa.2019.0791.
- 12. S. E. Rigby, S. D. Fay, S. D. Clarke, et al., "Measuring Spatial Pressure Distribution From Explosives Buried in Dry Leighton Buzzard Sand," *International Journal of Impact Engineering* 96 (2016): 89–104, https://doi.org/10.1016/j.ijimpeng.2016.05.004.
- 13. S. E. Rigby, A. Tyas, R. J. Curry, and G. S. Langdon, "Experimental Measurement of Specific Impulse Distribution and Transient Deformation of Plates Subjected to Near-Field Explosive Blasts," *Experimental Mechanics* 59, no. 2 (2019a): 163–178, https://doi.org/10.1007/s11340-018-00438-3.
- 14. A. D. Barr, S. E. Rigby, S. D. Clarke, D. Farrimond, and A. Tyas, "Temporally and Spatially Resolved Reflected Overpressure Measurements in the Extreme Near Field," *Sensors* 23, no. 2 (2023): 964, https://doi.org/10.3390/s23020964.
- 15. SSAB, "Datasheet for Domex 355 MC Steel," (2025), https://www.ssab.com/api/download?file=/api/sitecore/Datasheet/Get?key=27690dd1e2 6e44459e61286edb9dacd0_en.
- 16. S. E. Rigby, A. Tyas, R. J. Curry, and G. S. Langdon, "Near-Field Blast Loading and Transient Target Response: A Collaboration Between Sheffield and Cape Town," in *Advances in Engineering Materials, Structures and Systems: Innovations, Mechanics and Applications* (CRC Press, 2019b), https://doi.org/10.1201/9780429426506-130.
- 17. R. J. Curry and G. S. Langdon, "Transient Response of Steel Plates Subjected to Close Proximity Explosive Detonations in Air," *International Journal of Impact Engineering* 102 (2017): 102–116, https://doi.org/10.1016/j.ijimpeng.2016.12.004.
- 18. M. A. Sutton, W. Wolters, W. Peters, W. Ranson, and S. R. McNeill, "Determination of Displacements Using an Improved Digital Correlation Method," *Image and Vision Computing* 1, no. 3 (1983): 133–139.
- 19. M. A. Sutton, M. Cheng, W. H. Peters, Y. J. Chao, and S. R. McNeill, "Application of an Optimized Digital Correlation Method to Planar Deformation Analysis," *Image and Vision Computing* 4, no. 3 (1986): 143–150, https://doi.org/10.1016/0262-8856(86)90057-0.
- 20. W. Fourney, U. Leiste, R. Bonenberger, and D. Goodings, "Mechanism of Loading on Plates due to Explosive Detonation," *Fragblast* 9 (2005): 205–217.
- 21. V. Tiwari, M. A. Sutton, S. McNeill, et al., "Application of 3d Image Correlation for Full-Field Transient Plate Deformation Measurements During Blast Loading," *International Journal of Impact Engineering* 36, no. 6 (2009): 862–874, https://doi.org/10.1016/j.ijimpeng.2008.09.010.
- 22. V. Aune, E. Fagerholt, K. O. Hauge, M. Langseth, and M. Børvik, "Experimental Study on the Response of Thin Aluminium and Steel Plates Subjected to Airblast Loading," *International Journal of Impact Engineering* 90 (2016): 106–121, https://doi.org/10.1016/j.ijimpeng.2015.11.017.
- 23. R. J. Curry and G. S. Langdon, "The Effect of Explosive Charge Backing in Close-Proximity Air-Blast Loading," *International Journal of Impact Engineering* 151 (2021): 103822, https://doi.org/10.1016/j.ijimpeng.2021.103822.
- 24. International Digital Image Correlation (iDIC) Society, *A Good Practices Guide for Digital Image Correlation*, eds. E. M. C. Jones and M. A. Iadicola (International Digital Image Correlation (iDIC) Society, 2018), https://doi.org/10.32720/idics/gpg.ed1/print.format.
- 25. M. Rossi and F. Pierron, "On the Use of Simulated Experiments in Designing Tests for Material Characterization From Full-Field Measurements," *International Journal of Solids and Structures* 49, no. 3–4 (2012): 420–435, https://doi.org/10.1016/j.ijsolstr.2011.09.025.
- 26. É. Gagnon and J. Day, "The Practicality of Quality Assessment Metrics for Millimetre-Scale Digital Image Correlation Speckle Patterns," *Strain* 61 (2025): e12491, https://doi.org/10.1111/str.12491.
- 27. D. J. Atkinson, M. van Rooyen, and T. H. Becker, "An Artificial Neural Network for Digital Image Correlation Dynamic Subset Selection Based on Speckle Pattern Quality Metrics," *Strain* 60, no. 4 (2024): e12471, https://doi.org/10.1111/str.12471.
- 28. D. Miller, K. Shah, S. Sockalingam, and M. A. Sutton, "Uncertainty Analysis of Acceleration and Velocity Fields Measured via DIC," *International Journal of Mechanical Sciences* 2025 (2025): 110599, https://doi.org/10.1016/j.ijmecsci.2025.110599.
- 29. R. Balcaen, P. Reu, P. Lava, and D. Debruyne, "Stereo-DIC Uncertainty Quantification Based on Simulated Images," *Experimental Mechanics* 57 (2017): 939–951, https://doi.org/10.1007/s11340-017-0288-9.
- 30. R. Kaufmann, S. Olufsen, E. Fagerholt, and V. Aune, "Reconstruction of Surface Pressures on Flat Plates Impacted by Blast Waves Using the Virtual Fields Method," *International Journal of Impact Engineering* 171 (2023): 104369, https://doi.org/10.1016/j.ijimpeng.2022.104369.
- 31. R. Kaufmann and V. Aune, "Advancements in Full-Field Pressure Reconstruction of Water-Wave Impact," *Journal of Sound and Vibration* 608 (2025): 119048, https://doi.org/10.1016/j.jsv.2025.119048.
- 32. A. Tyas, J. J. Reay, S. D. Fay, et al., "Experimental Studies of the Effect of Rapid Afterburn on Shock Development of Near-Field Explosions," *International Journal of Protective Structures* 7, no. 3 (2016): 452–465, https://doi.org/10.1177/2041419616665931.

Strain, 2025 27 of 28

- 33. N. Jacob, G. N. Nurick, and G. S. Langdon, "The Effect of Stand-Off Distance on the Failure of Fully Clamped Circular Mild Steel Plates Subjected to Blast Loads," *Engineering Structures* 29, no. 10 (2007): 2723–2736, https://doi.org/10.1016/j.engstruct.2007.01.021.
- 34. G. S. Langdon, A. Ozinsky, and S. Chung Kim Yuen, "The Response of Partially Confined Right Circular Stainless Steel Cylinders to Internal Air-Blast Loading," *International Journal of Impact Engineering* 73 (2014): 1–14, https://doi.org/10.1016/j.ijimpeng.2014.05.002.
- 35. B. McDonald, "Characterising Material Effects in Blast Protection" (Thesis, RMIT University, 2019), https://doi.org/10.25439/rmt.27582567.
- 36. S. McKown, Y. Shen, W. K. Brookes, et al., "The Quasi-Static and Blast Loading Response of Lattice Structures," *International Journal of Impact Engineering* 35, no. 8 (2008): 795–810, https://doi.org/10.1016/j.ijimpeng.2007.10.005.
- 37. B. McDonald, H. Bornstein, A. Ameri, A. Daliri, and A. C. Orifici, "Plasticity and Ductile Fracture Behaviour of Four Armour Steels," *International Journal of Solids and Structures* 176–177 (2019): 135–149, https://doi.org/10.1016/J.IJSOLSTR.2019.05.013.
- 38. S. Chung Kim Yuen, G. N. Nurick, G. S. Langdon, and Y. Iyer, "Deformation of Thin Plates Subjected to Impulsive Load: Part III An Update 25 Years on," *International Journal of Impact Engineering* 107 (2017): 1339–1351, https://doi.org/10.1016/j.ijimpeng.2016.06.010.
- 39. A. Tyas, "Near-Field High Explosive Blast Loading: The Challenges for Measurement and Prediction," Proc. 5th Int Conf Protective Structures, 19-23 Aug 2018, Poznan University of Technology, Poland, (2018).
- 40. H. G. Hopkins, "On the Plastic Theory of Plates," *Proceedings of the Royal Society of London* A241 (1957): 153–179, https://doi.org/10.1098/rspa. 1957.0120.
- 41. N. Jones, Structural Impact, 2nd ed. (Cambridge University Press, 2011).
- 42. M. A. Wiehahn, G. N. Nurick, and H. C. Bowles, "Some Insights Into the Mechanism of the Deformation and Tearing of Thin Plates at High Strain Rates Incorporating Temperature Dependent Material Properties," WIT Transactions on the Built Environment 48 (2000): 12, https://doi.org/10.2495/SU000031.
- $43. G. N. Nurick, M. E. Gelman, and N. S. Marshall, "Tearing of Blast Loaded Plates With Clamped Boundary Conditions," {\it IJIE}\ 18, no.\ 7-8 (1996): p803-p827, https://doi.org/10.1016/S0734-743X(96)00026-7.$